Pacific Northwest
NATIONAL LABORATORY

Proudly Operated by **Battelle** *Since 1965*

Annual Report for the QCL Calibration Project

March 2015

BE Bernacki   TL Myers
CS Brauer   MS Taubman
BD Cannon   CG Anderson

U.S. DEPARTMENT OF
ENERGY

Annual Report for the QCL Calibration Project

BE Bernacki   TL Myers
CS Brauer   MS Taubman
BD Cannon   CG Anderson

March 2015

Summary

Under the Quantum Cascade Laser (QCL) Calibrations project, Pacific Northwest National Laboratory (PNNL) is collaborating with Utah State University and Space Dynamics Laboratory to design, build, and test a QCL calibration source system suitable for insertion into remote sensing platforms. In FY14, the second year of this project, PNNL completed the radiation testing of QCLs using radiation levels that are typical for a space environment. These tests involved both 64-MeV protons, and 1.17-MeV and 1.33-MeV gamma rays. No changes were observed above the measurement uncertainty indicating that QCLs are viable sources for space-based missions. High-level testing was also carried out with gamma rays to determine if QCLs are sensitive to high doses of gamma radiation. After an accumulated dose of 1.5 Mrad(Si), the QCLs continue to demonstrate high performance although a small increase in threshold current, $0.11 \pm 0.14\%$ and $0.51 \pm 0.15\%$ for M1244D and M664M, respectively, was observed. At this stage, it is unclear if this small increase is from the radiation exposure, because generally it is within the observed experimental uncertainty, which is most likely because of mechanical changes through repeated mounting cycles. There was also some accidental damage to the laser chips and their front facets from the extensive but necessary handling of the devices during these tests. Regardless, the QCLs are robust and should not be susceptible to degradation for most missions.

Images of the beam output from an integrating sphere showed that continuous wave (cw) operation of the QCLs led to speckle noise in the beam profile because of the coherence of the QCL. The contrast of this speckle, and hence its impact, was decreased by more than an order of magnitude by modulating the current of the QCL. The typical current modulation frequency was 40 kHz for this work for reasons associated with current controller performance, although another contrast reduction of a factor of two was shown by increasing the modulation frequency to 100 and 200 kHz. Higher modulation frequencies may be preferable at some point.

Images of the beam output also showed the integrating sphere effectively homogenizes the laser intensity profile, and the compound parabolic concentrator (CPC) reduces the divergence of the light exiting the sphere. Although this testing used collimated QCLs, the final design will use uncollimated QCLs to reduce optical feedback effects. To ensure efficient coupling of the lasers into the sphere, a tapered light guide input has been designed to minimize the probability that direct and singly scattered rays could exit the sphere and create hot spots in the intensity profile.

Acronyms and Abbreviations

CCD	charge-coupled devices
CPC	compound parabolic concentrator
cw	continuous wave
FP	Fabry-Perot
HHL	high head load
HS	heatsink
IR	infrared
kHz	kilohertz
krad(Si)	kilorad unit; radiation absorbed dose in silicon
L-I	power versus current (curve)
MeV	Mega electron volt unit
Mrad(Si)	Megarad unit; radiation absorbed dose in silicon
NA	numerical aperture
PNNL	Pacific Northwest National Laboratory
QCL	quantum cascade laser
R	roentgen
Rad	Radiation abosorbed dose
SDL	Space Dynamics Laboratory
USU	Utah State University

Contents

Figures

Tables

1.0   Introduction

The goal of this project is to provide enhanced infrared (IR) calibration sources to enable collection of high-quality data from IR sensors used for national security applications. For this effort, Pacific Northwest National Laboratory (PNNL) is collaborating with Utah State University (USU) and Space Dynamics Laboratory (SDL), who have extensive experience with designing, building, and testing space-based instrumentation. The overall objective for this project is to design, construct, and test calibrators based on quantum cascade lasers (QCLs) for insertion into remote sensing platforms. Much of the work to date has focused on developing space-qualified QCLs and drivers. In particular, USU and SDL have focused much of their efforts on developing a space-qualified driver by modifying the current controller developed previously at PNNL (Taubman 2011; Taubman et al. 2014) and selecting parts that are amenable to space qualification; that is, radiation tolerant. The other principal focus of this project has been to demonstrate that QCLs are not susceptible to cumulative radiation levels typically encountered by electronic components in space environments. Thus, much of the work in FY13 and FY14 involved exposing the QCLs to two different types of radiation: (1) 64-MeV protons and (2) 1.17-MeV and 1.33-MeV gamma rays.

Another key component for this project is the source system design. Both PNNL and USU have modeled several variants to determine the optimal layout for providing uniform optical output. Although USU is focusing on a source system involving a single QCL, PNNL is pursuing a source system combining at least three QCL sources that can be selected by the user to illuminate the instrument under calibration for radiometric calibration (and perhaps wavelength calibration). The design, which must provide a uniform irradiance pattern, involves coupling the laser sources into an integrating sphere and then transforming the output emission angle of the sphere using a compound parabolic concentrator (CPC). Care must be taken to eliminate the possibility of light directly exiting from the exit port of the integrating sphere as well as single scattered rays that give rise to inhomogeneity in the output intensity and produce hot spots in the output intensity profile. One potential solution to eliminate this effect is to inject the laser light through a rectangular beam homogenizer in combination with strategically placed baffles inside of the integrating sphere. This approach is discussed in this report.

The calibration source must also lack spatial or temporal coherence. QCL sources, however, are highly polarized point sources that possess temporal and spatial coherence and emit with a highly directional quasi-Gaussian output. The coherence of the QCL beam enables the beam to interfere with itself to cause speckle, which can produce a non-uniform irradiance pattern in the system. This coherence must be mitigated in order to avoid calibration errors. Thus, the QCL source must be transformed to have a uniform output with reduced coherence effects (speckle) and random polarization. We have proposed to reduce the laser coherence by modulating the laser current to average out the interference effects. This technique has been tested, and the results are presented in this report.

1.1 Report Layout

This report details the work performed on the QCL Calibrations project during FY14. Section 2.0 discusses radiation tests performed on a number of selected QCLs, to evaluate impact on operation and lifetime. Section 3.0 discusses beam homogenization for the source system design, while Section 4.0 discusses the approach for coherence mitigation. Section 5.0 discusses further beam conditioning through CPC performance. Finally, a summary is provided in Section 6.0, and references are provided in Section 7.0.

2.0   Radiation Testing

To determine if radiation will impair the operation or lifetime of QCLs, part of our work has involved exposing QCLs to different forms of radiation that are expected during a typical mission. This testing was started in FY13 (Bernacki et al. 2014) and involved exposing the QCLs to both proton and gamma radiation. The proton irradiation testing was carried out at the University of California at Davis Crocker Nuclear Laboratory in which the samples are placed in a 64-MeV proton beam. This proton testing was made feasible by piggybacking on experiments performed by SDL in which they have been testing the effects of proton exposure on charge-coupled devices (CCDs). The gamma irradiation work was performed at PNNL using a Cobalt-60 source that produces gamma rays at 1.17 MeV and 1.33 MeV. This Co-60 source is part of the PNNL radiation dosimeter calibration facility and provides a low-cost method for testing.

Most of the testing involved exposure to radiation doses typical of space missions, as discussed in Section 2.1; tests using radiation orders of magnitude higher than this, in order to provide more complete understanding of radiation damage of QCLs, are discussed in Section 2.3. Although the SI unit for absorbed dose is the gray (Gy), the rad (radiation absorbed dose) is commonly used. In this report, doses are reported as krad(Si) and Mrad(Si) for the radiation absorbed relative to silicon, which isn't the actual material for the QCLs but is commonly used to represent semiconductor devices.

It should be noted that throughout this report, unless otherwise stated, uncertainties are quoted as 2σ, or twice the standard reported error (σ). This fact will be restated for clarity whenever uncertainties are discussed. Uncertainty bounds of $\pm 2\sigma$ are often used because they give more complete bounding of data variation (95.4%) as opposed to the standard error, σ ($\pm\sigma$ corresponds to 68.2%). Also, the process of mounting a C-mount (with or without QCL attached), performing measurements (or not, as the case may be), and then dismounting the C-mount, is from here on referred to as a "mounting cycle."

2.1   Space Qualification Testing

We tested seven Fabry-Perot QCLs from two vendors using radiation levels that are typical for a seven-year mission. The exposure data for the proton and gamma testing are shown in Tables 1 and 2, respectively. The total radiation doses used in this study vary between 20 krad(Si) and 46.3 krad(Si). Six of the QCLs were exposed to both a 10-krad(Si) dose of protons as well as a total accumulated dose of 26.3 krad(Si) for gamma-rays delivered over three steps. Two QCLs were exposed to two doses of protons for a total accumulated proton dose of 20 krad(Si); one of these QCLs was also exposed to gamma radiation for a total accumulated dose of 46.3 krad(Si). For a comparison, the total daily dose for a spacecraft at an altitude of 500 km and 60° inclination, which is typical of a low earth orbit, is calculated to be 13.0 rads(Si); over a seven-year timeframe the accumulated dose would be 33.3 krads(Si) (Stassinopoulos and Raymond 1988); thus, these total dose amounts are within the range of total accumulated doses typically experienced by electronic components in a space environment. The radiation levels vary with altitude, angle of inclination, solar activity, and spacecraft shielding, which is typically around 100–250 mils.

Table 1. Proton Beam Exposure Data Using a 64-MeV Proton Beam

Date	QCLs	Fluence (p/cm^2)	Irradiation Time (minutes)	Absorbed Dose (krad)
10/23/2012	Ham-Ce, Ham-Cf	7.50E+10	Not provided	10
1/03/2013	Ham-Ce, Ham-Cf	7.50E+10	296	10
8/26/2013	M664O, M1244C-D, M1244F-G	7.50E+10	599	10

Table 2. Gamma Radiation Exposure Data Using the 318-528 Source at PNNL

Date	QCLs	Distance from Source (m)	Exposure Rate (R/h)	Irradiation Time (minutes)	Absorbed Dose (krad)
3/06/2013	Ham-Ce, M664O	0.788	10,000	60.0	8.77
3/29/2013	Ham-Ce, M664O	0.785	10,000	60.0	8.77
4/11/2013	Ham-Ce, M664O	0.785	10,000	60.0	8.77
12/30/2013	M1244C,D,F,G	1.0	5560	107.91	8.77
1/24/2014	M1244C,D,F,G	1.0	5512	108.86	8.77
2/12/2014	M1244C,D,F,G	1.0	5474	109.60	8.77

Five of the QCLs used in this testing are from Maxion Technologies (now Thorlabs). These devices incorporate an active region based on a four-level system, having a double phonon resonance for the lower level (Hofstetter et al. 2001). Fabrication of the devices is similar to that shown in Leavitt et al. (2010)—the QCLs are fabricated as double-channel ridge lasers, which helps limit lateral current spreading in the device. All QCLs are mounted epi-down on a copper C-mount. Additional design details for these QCLs are provided in Table 3.

Table 3. Design Details for Some of the QCLs Used in the Radiation Testing

QCL	Wave-length (μm)	# Wells in Injector Region	Strained	GaIn(x)As	AlIn(y)As	Ridge width (μm)	EP Au Thickness (μm)	Rear Facet*	Solder to HS
M577G	5.4	8	Yes	0.678	0.635	6.6	4	HR (M)	Pb/Sn
M664O	8.2	7	No	0.532	0.523	14	3.5	HR (M)	Pb/Sn
M1244C	4.8	8	Yes	0.720	0.340	8.9	5	HR (D)	Ag/Sn
M1244D	4.8	8	Yes	0.720	0.340	8.9	5	HR (D)	Ag/Sn
M1244F	4.8	8	Yes	0.720	0.340	8.9	5	Unc	Ag/Sn
M1244G	4.8	8	Yes	0.720	0.340	8.9	5	Unc	Ag/Sn

*M corresponds to Y_2O_3/Ti/Au/Y_2O_3, D corresponds to an all-dielectric coating, Unc is uncoated.

The performance of the QCL is measured prior to and after the radiation exposure using the testing station that has been discussed in Myers et al. (2013). The thermopile and laser mount are shown in Figure 1, which is placed inside a custom Styrofoam enclosure. Fixtures are used to help maintain precise alignment when the QCL is removed from the laser mount.
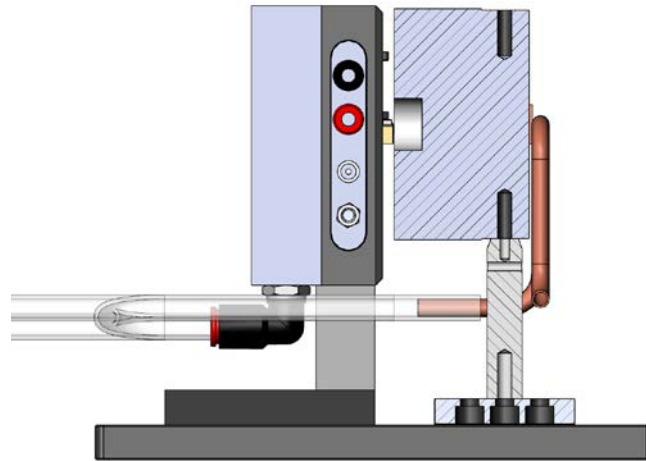
Figure 1.   Schematic of the Experimental Set-up Showing the Temperature-Controlled Laser Mount and a Thermopile with a 19-mm Aperture Used to Measure the Output Power. A QCL attached to a C-mount is fastened to the mount. Water cooling is used to stabilize the thermopile temperature.

The QCLs are ramped over five current levels above threshold and the output power is measured at each step with a thermopile to generate a power versus current (L-I) curve. The threshold current and slope efficiency are calculated by performing a linear regression on the data points of the L-I curves. These three parameters—output power, threshold current, and slope efficiency—are used to monitor any effects from radiation exposure. An increase in threshold current and a decrease in slope efficiency are indicative of degradation to the device structure. Further details about the radiation testing can be obtained from Bernacki et al. (2014) and Myers et al. (2013).

As discussed in the FY13 report (Bernacki et al. 2014), repeated measurements in which the laser was dismounted and remounted to the temperature-controlled laser mount showed that the uncertainties in the output power, threshold current, and slope efficiency were much higher than that measured when the QCL is left attached to the mount. This increased variability is most likely due to changes in thermal contact between the QCL and the laser mount. Because the QCL temperature is regulated by controlling the temperature of a thermistor embedded in the plate of the laser mount, changes in thermal contact between the QCL and the mount will result in changes to the temperature of the QCL active region. Minor changes in the active region temperature will cause fluctuations in the output power as well as threshold current. Thus, in order to address this issue, we measured the variability from dismounting and remounting the QCL and C-mount for a set of ten measurements.

For these measurements, a set procedure was followed: the laser mount surface and the back of the C-mount were cleaned with methanol, and the C-mount (and QCL) was attached to the laser mount using a

torque wrench to tighten the mounting screw to 32 oz-in. Figure 2 shows the first ten measurements for the control QCL, M577G. The variability for the threshold current over these ten measurements is ±1.1 mA, giving an uncertainty of ±0.2%; the variability for the slope efficiency is ±13 mW/A, giving an uncertainty of ±2%. On the other hand, the variability is at least an order of magnitude lower when the QCL is not removed from the mount. For example, the average variability for the threshold current over 26 L-I cycles is only ±0.1 mA, and the variability for the slope efficiency is only ±0.4 mW/A.
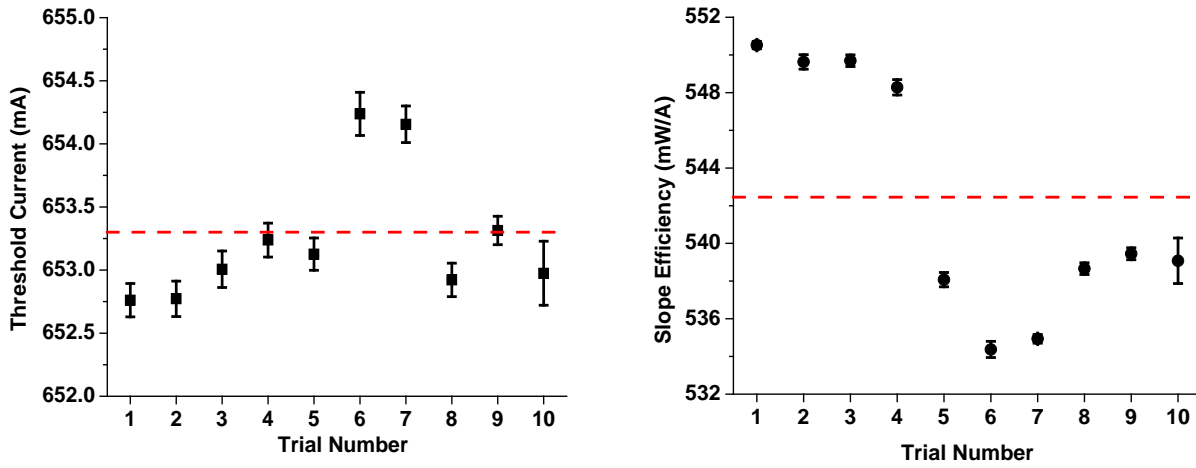
Figure 2.   Plots Showing the Observed Variability of Threshold Current (left) and Slope Efficiency (right) over Ten Dismount and Remount Cycles for the Control QCL, M577G. The error bars represent ±2σ of the 26 L-I cycles. The dashed lines represent the average of these ten measurements.

Table 4 shows the average threshold current and slope efficiency over all ten measurements for M577G as well as the four M1244 QCLs that are used for the second phase of radiation testing experiments. The average uncertainty over all five QCLs was ±1.2 mA for the threshold current and ±18 mW/A for the slope efficiency. Thus, minor changes in threshold current (<0.3%) and slope efficiency (<2%) will be hard to detect. These measurements further support the claim that any variability observed with the initial round of testing presented in Section 3.2 is within measurement error.

Table 4. Average Threshold Current and Slope Efficiency for Five QCLs over Ten Measurements

QCL	Average Threshold Current (mA)	Uncertainty (%)	Average Slope Efficiency (mW/A)	Uncertainty (%)
M577G - Control	653.3 ± 1.1	0.17	542 ± 13	2.4
M1244C	459.4 ± 0.7	0.15	1490 ± 5	0.3
M1244D	459.4 ± 0.5	0.11	1538 ± 35	2.3
M1244F	613.2 ± 2.5	0.41	933 ± 19	2.0
M1244G	613.5 ± 1.1	0.18	992 ± 18	1.8

The fractional changes in threshold current and slope efficiency of the QCLs after exposure to proton radiation are shown in Figure 3. The early measurements for Ham-Ce and Ham-Cf are discussed in more detail in the FY13 report (Bernacki et al. 2014). These early studies involved fewer measurements, indicating that the potential variability resulting from thermal contact changes between the C-mount and the temperature-controlled mount may not be accurately captured in the standard deviation. Generally, QCL threshold and slope efficiency data are presented as averages taken over ten mounting cycles. For Ham-Ce and Ham-Cf, however, fewer measurements were taken—for Ham-Ce only five measurements were used prior to proton exposure, and then three measurements were used after proton exposure; for Ham-Cf only one average of six measurements were used prior to proton exposure, and then two measurements were used after proton exposure (see Bernacki et al. 2014 report). Later, an average of ten measurements was used to better account for the variability that results from dismounting and remounting the QCL to the temperature-controlled mount. The largest increase in threshold current of all the tested QCLs was observed for Ham-Cf; however, due to the limited number of measurements after proton exposure (only two), this change is most likely due to measurement variability and not due to radiation exposure. Ham-Ce, which is similar to Ham-Cf, showed no measurable change in threshold current. Unfortunately, Ham-Cf was dropped during the testing program and suffered mechanical damage to the front facet so that it no longer operated and had to be removed from the testing program. Four of the QCLs showed a decrease in threshold current, although these changes are within the measurement uncertainty. Thus, no changes were observed beyond measurement uncertainty, indicating QCLs are robust to proton exposure at these radiation levels, which are typically used for space qualification.
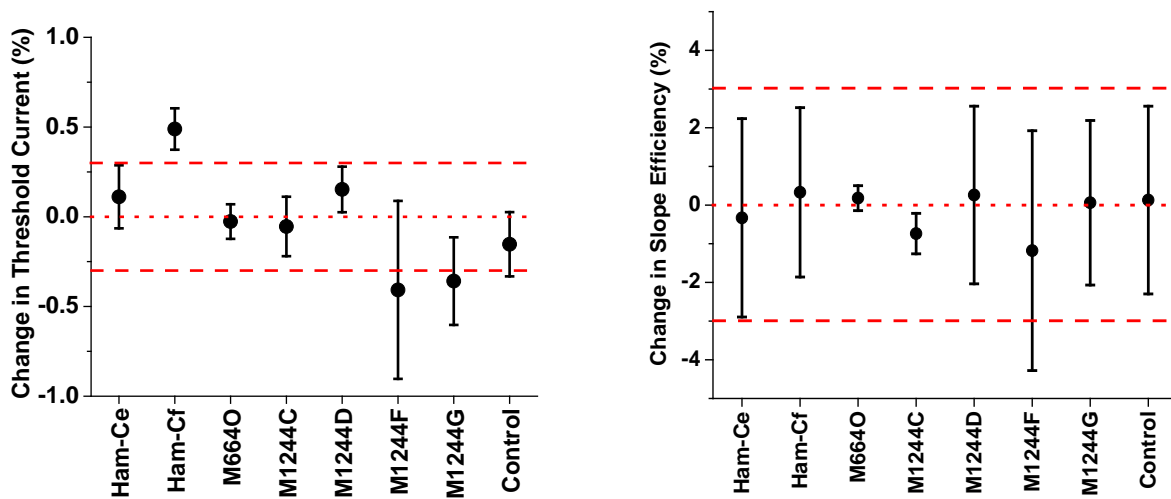
Figure 3. Plots Showing Fractional Change in Threshold Current (left) and Slope Efficiency (right) after a Proton Dose of 10 krad(Si). Both Ham-Ce and Ham-Cf had already been exposed to a proton dose of 10 krad(Si), and M664O had already been exposed to 46.3 krad(Si) of gamma-rays prior to these tests. The red dashed lines show uncertainties of ±2σ.

The QCLs were also exposed to gamma radiation in a series of three steps for an accumulated dose of 26.3 krad(Si). Figure 4 shows the fractional changes in threshold current (left graph) and slope efficiency (right graph) for all six devices as well as the control QCL. The error bars were calculated using error propagation. None of the devices show a measurable increase in threshold current or slope efficiency after the gamma exposure. M1244F as well as M1244G do not have an HR coating and greater variability is

usually observed; this increased variability is presumably due to half of the light exiting the rear facet, which can lead to scattering off of the laser mount as well as optical feedback effects.
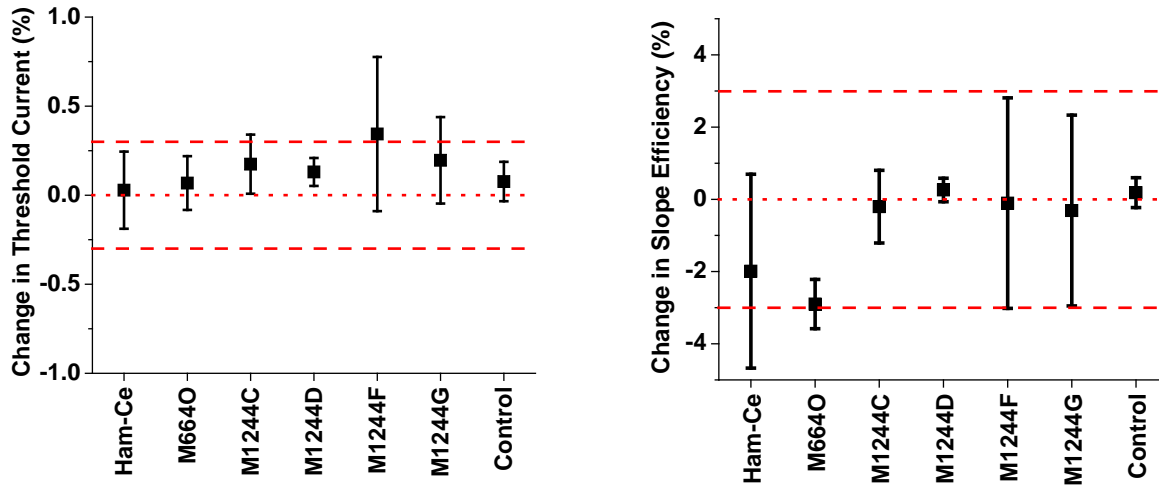
Figure 4.   Fractional Change in Threshold Current (left) and Slope Efficiency (right) after a Total Accumulated Gamma Dose of 26.3 krad(Si). The red dashes lines the uncertainties of ±2σ.

These tests clearly show that Fabry-Perot (FP) QCLs from two different vendors continued to operate after exposure to radiation levels likely to be encountered for most space-based missions. Six of the QCLs were exposed to both high-energy 64-MeV protons and gamma rays; one QCL was exposed only to 64-MeV protons. Minimal changes in output power, threshold current, and slope efficiency were observed. These studies show that QCLs continue to demonstrate excellent performance both after proton and gamma irradiation, making them a viable choice for use in space missions.

2.2 Technical Challenges

A typical mounting of a QCL on a C-mount is shown in Figure 5. The C-mount, approximately 0.25-inch wide and 0.3-inch long, provides several technical challenges for the radiation testing procedures performed under this project. First, the C-mount does not provide protection for the delicate laser chip, which remains fully exposed. This leaves the laser facets sensitive to particulate accumulation, especially during operation. Moreover, the facets and connections are prone to mechanical damage. The greatest risk to the devices is thus introduced through physical handling. Extreme care must be taken to avoid accidental damage by touching the laser facet. M577G (the control QCL) and M664O were both damaged in this manner this FY, while being attached to the laser mount.
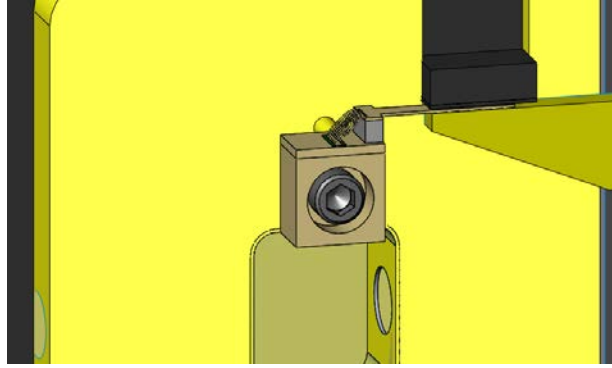
Figure 5. CAD Drawing of C-mount with QCL Attached to Temperature-Controlled Mount and Associated Connections

Gloves are worn during mounting procedures to prevent the deposition of skin oils and other contaminants. Efficient heat transfer requires good thermal contact between the C-mount and the heatsink, which is achieved by securing them to each other with a single #2-56 mounting screw as shown in Figure 5. Thermal grease cannot be used to improve the thermal contact because it can creep and contaminate the laser facet.

2.2.1 Physical Handling of Devices

Micrographs were recorded before and after the radiation exposure testing. Figure 6 shows micrographs of the front facet of M1244C before and after radiation exposure. Damage is primarily observed in the InP substrate and is most likely due to damage from handling the QCLs during attachment to the temperature-controlled mount. Even though care is exercised, these lasers are handled frequently, increasing the risks. All the QCLs showed similar scratches and chips, or other defects in the substrate (even the control QCL, which is not exposed to radiation). Except for the devices from Hamamatsu, all of the QCLs were mounted epi-down on an AlN submount which is then mounted onto the C-mount.
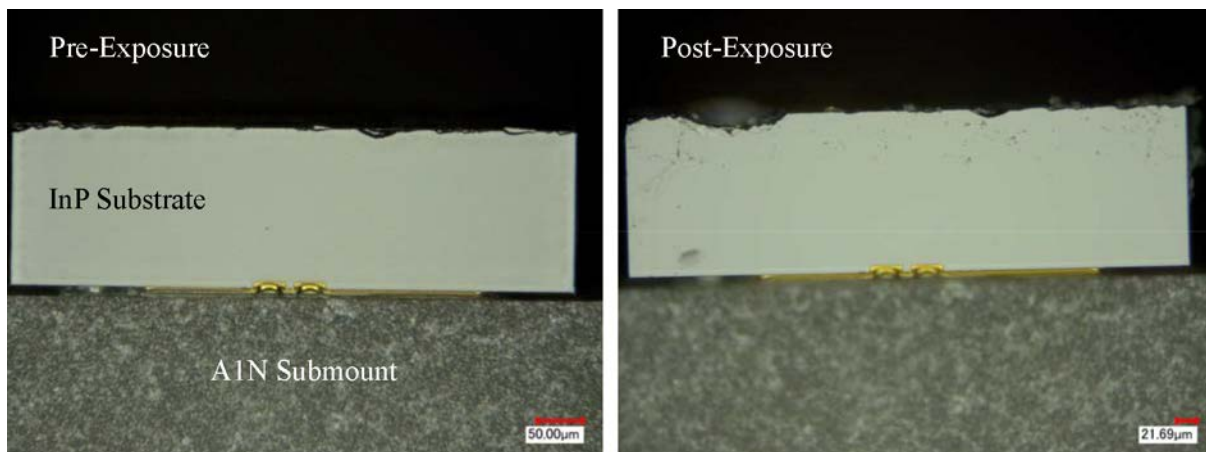
Figure 6. Micrographs of the Front Face of M1244C before (left), and after (right) Radiation Exposure and 60 Mount-Dismount Cycles

Micrographs taken of the back faces of C-mounts (containing QCLs) shown in the top two and bottom left panels of Figure 7 indicate that the gold coating appears to be rubbing off due to repeated mount-dismount cycles. This wear could conceivably increase the resistance of the thermal contact, reducing its heat dissipating capacity, thus affecting QCL threshold current. Unfortunately, photos were not taken of the C-mount rear faces prior to mounting.

The lower right panel of Figure 7 shows a micrograph of the rear face of a C-mount for a QCL recently purchased from ThorLabs, which has been neither tested nor mounted at PNNL. Ideally, the mounting surface should be finely milled or lapped to provide good thermal contact, but the surface of this C-mount appears to be rough and shows some minor scratches, even before it was bolted to a heatsink. However, there is less wear compared to those micrographs seen in the first three panels of Figure 7, supporting the supposition that this damage occurs from repeated mounting.

One option to improve the thermal contact is to use a silver-filled epoxy between the C-mount and the heatsink. This option, however, has not been tested. If silver-filled epoxy were to be used, it should be a "space-qualified," low-outgassing epoxy, to avoid contamination of the laser facets (Epoxy Technology H21D, for example).
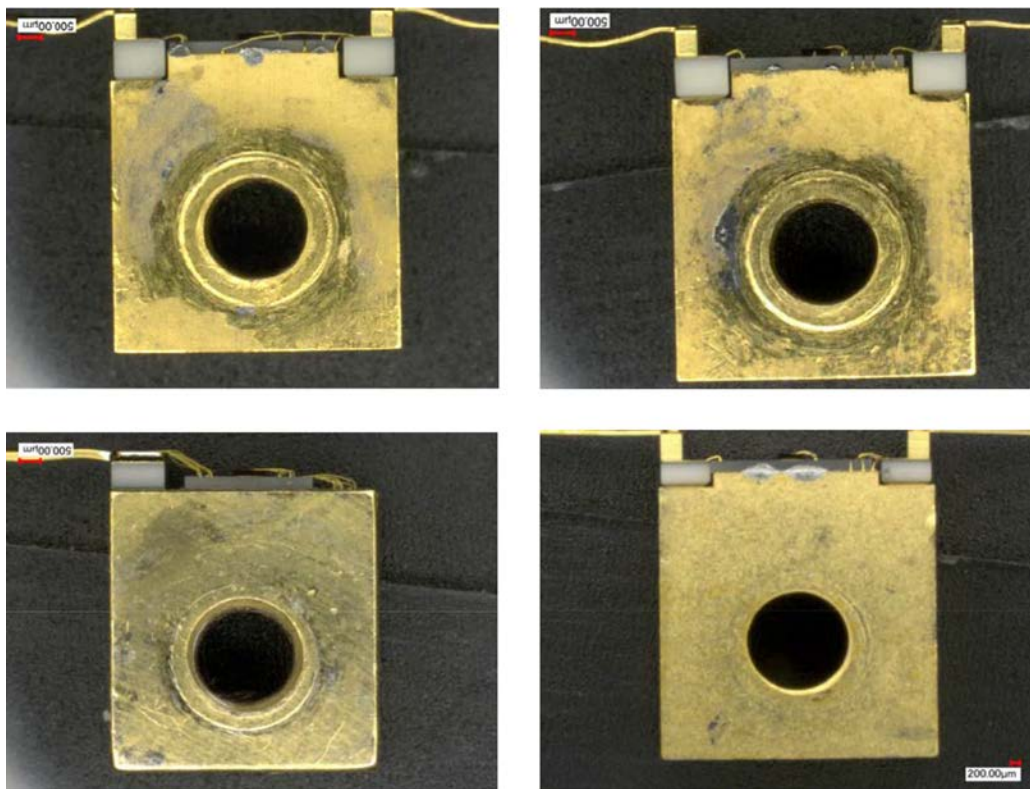
Figure 7.   Micrographs of Back Faces of C-mounts for M1244C (top left) and M1244G (top right) after Radiation Testing, and More Than 60 Mounting Cycles and for the control QCL, M577G, (bottom left) as well as a Recently Purchased Device from Thorlabs, QF9150CM1BS, Examined Before any Mounting or Testing at PNNL (bottom right).

2.2.2   Degradation of C-mount Surface

To further investigate the effect of mount-dismount cycles on C-mounts, we conducted three different tests on blank C-mounts (i.e., no QCL attached): (1) a C-mount was mounted and dismounted 20 times, during which, the back face of the C-mount was *not* cleaned with methanol between mountings (see Figure 8); (2) a C-mount was mounted and dismounted 20 times, during which the back face *was* cleaned with methanol using a cotton swab (see Figure 9); and (3) a C-mount was mounted and dismounted 20 times using a thermal contact pad[a] between the two surfaces, *without* cleaning the back face with methanol (see Figure 10). Photographs were taken of the rear face of the C-mounts before and after these tests. The best results were achieved using the thermal contact pads, which appear to prevent excessive wear on the C-mount. Unfortunately, the threshold current increased significantly due to inefficient heat transfer when using these pads, so that this method could not be used.

What is clear from the above-described tests is that it only takes 20 mount-dismount cycles for the C-mount rear face to show non-negligible signs of wear and discoloration. The radiation testing procedures have required over 60 mount-dismount cycles; it is clear that the handling of the C-mounts induces effects that could compromise thermal contact and reliability.
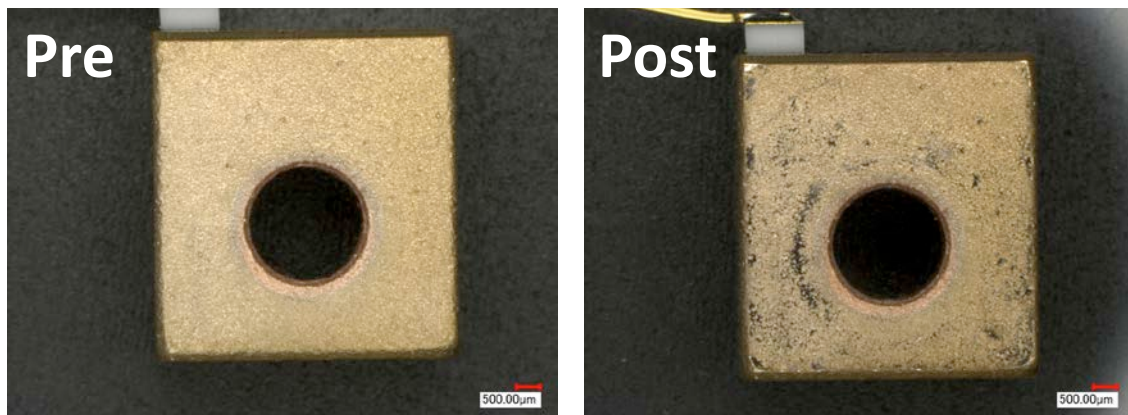
Figure 8.   Pre (left) and Post (right) Back Surface of C-mount after Mounting and Dismounting the C-mount from the Temperature-Controlled ILX Mount 20 Times without Cleaning the Surface Between Cycles

---

(a) The thermal contact pads were Tgard[TM] 220, which consist of a silicon/boron nitride composite. They are 0.020-in. thick with a thermal conductivity of 5 W/mK (thermal conductive insulator).
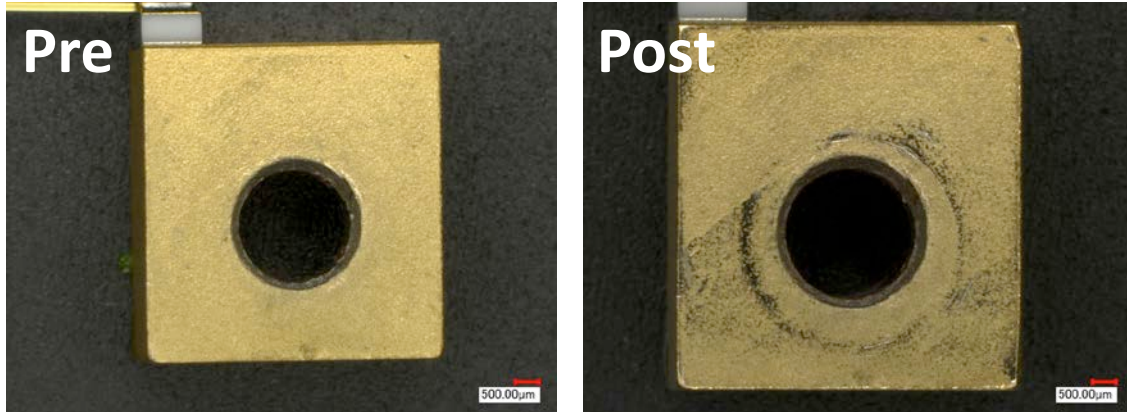
Figure 9.   Pre (left) and Post (right) Back Surface of C-mount after Mounting and Dismounting the C-mount from the Temperature-Controlled ILX Mount 20 Times in which the Back Surface of the C-mount is Cleaned with Methanol Each Time
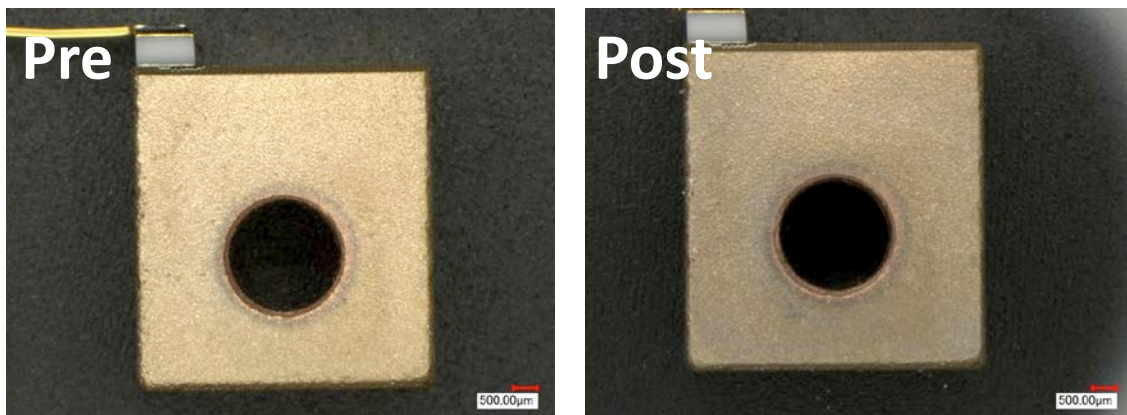
Figure 10.   Pre (left) and Post (right) Back Surface of C-mount after Mounting and Dismounting the C-mount from the Temperature-Controlled ILX Mount 20 Times Using a Thermal Contact Pad Each Time

2.3   Modifications to Testing Station

The test set-up for the QCL power measurements was modified in May 2014. Originally, a plastic container housing the power meter head and the laser mount was placed inside a Stryofoam container, and a separate Styrofoam container housed the power meter readout and the custom current controller, QCL6N. The new set-up shown in Figure 11 uses a double Styrofoam housing for the power measurements: a smaller Styrofoam enclosure houses the power meter head and the laser mount that is placed inside a larger Styrofoam box that includes the QCL6N and the power meter readout. A recently purchased power meter head has replaced the older power meter head that used water-cooled copper tubing (see Figure 1) to control the temperature; now, a metal cooling jacket provided by USU encloses the power meter head (see right panel in Figure 11). The outer Styrofoam box is placed inside a cardboard box.

The modified testing station shows similar long-term results, as shown in Table 5 in which the data from March 27-31 is from the original testing station, and the data from June 3-7 is from the modified testing station shown in Figure 11.
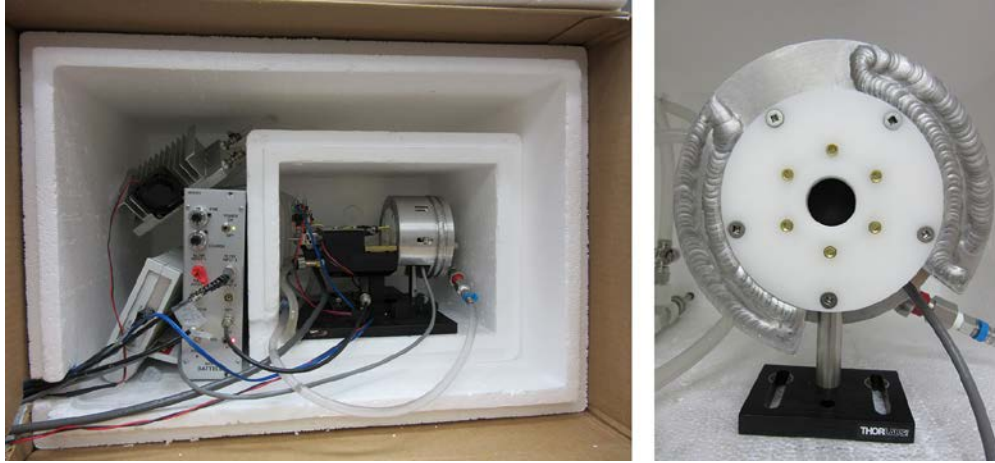
Figure 11.   Picture of Temperature-Controlled Laser Mount, Power Detector, and Current Controller in Double Styrofoam Box Enclosure (left) and Close-Up of Power Meter with Water Cooling Jacket (right)

Table 5. Test Results of Using Modified Testing Station over 1164 Cycles

Run #	R2	R3	R4	R5	R6	Threshold	Slope Eff.
March 27–March 31	4.953 ±0.026	10.744 ±0.025	16.685 ±0.028	22.796 ±0.027	27.777 ±0.026	460.64 ±0.03	1565.3 ±0.2
June 3–June 7	5.047 ±0.026	11.401 ±0.024	17.901 ±0.025	24.580 ±0.030	29.995 ±0.035	461.05 ±0.03	1710.9 ±1.3

2.4   High Radiation Testing

Additional testing using the Co-60 source at PNNL was performed in order to test if a high dose caused radiation damage in the QCL structure. Two QCLs (M664M and M1244D) were exposed to gamma radiation in three steps at a dose of 500 krad(Si) per step for a total accumulated dose of 1.5 Mrad(Si). The parameters used for the radiation testing are shown in Table 6. M1244D has already been exposed to 10 krad(Si) of protons and 46.3 krad(Si) of gamma-rays as discussed in Section 2.1. The design details for the QCLs used in this testing are shown in Table 7.

Table 6. Gamma Radiation Exposure Data using the 318-528 Source at PNNL

Date	Distance from Source (m)	Exposure Rate (R/h)	Irradiation Time (minutes)	Absorbed Dose (krad)
8/4/2014	0.367	39,000	877.2	500.0
8/15/2014	0.365	39,279	872.8	501.1
9/16/2014	0.365	38,824	881.1	500.0

A control QCL is evaluated in tandem with the QCLs exposed to radiation; this QCL was not subject to the stresses of radiation dose or transportation and is used as an indicator for changes in the test measurement set-up. Unfortunately, after the second radiation exposure, the control QCL (M577G) was damaged after only four measurements so that a new QCL, M665B, had to be used as the control. This delayed the testing of the third gamma dose; thus, additional testing was carried out on M1244D and M664M prior to the third gamma exposure. Table 8 provides the average values for the threshold current and slope efficiency before and after each gamma dose.

Table 7. Design Details for Some of the QCLs used in the Radiation Testing

QCL	Wave-length (μm)	# Wells in Injector Region	Strained	GaIn(x)As	AlIn(y)As	Ridge Width (μm)	EP Au Thickness (μm)	Rear Facet*	Solder to HS
M577G	5.4	8	Yes	0.678	0.635	6.6	4	HR (M)	Pb/Sn
M665B	8.6	7	No	0.532	0.523	11.8	5	HR (M)	Ag/Sn
M664M	8.2	7	No	0.532	0.523	12	3.5	HR (M)	Pb/Sn
M1244D	4.8	8	Yes	0.720	0.340	8.9	5	HR (D)	Ag/Sn
*M corresponds to Y_2O_3/Ti/Au/Y_2O_3, D corresponds to an all-dielectric coating.									

The changes in threshold current and slope efficiency for each dose are shown in Figure 12. The changes for the third step for M664M and M1244D and M665B are calculated by using the average measurements prior to exposure (in Table 8, before 3rd gamma dose). The values for M577G are used for the first two steps for the control laser and then the values for M665B are used for the third step.

Both M664M and M1244D had a larger increase in threshold current than the control QCL as seen in the right graph of Figure 12. The fractional change in threshold current after a total accumulated dose of 1.5 Mrad(Si) is $0.11 \pm 0.14\%$ and $0.51 \pm 0.15\%$ for M1244D and M664M, respectively. The measured change in threshold current for M1244D is clearly within the measurement uncertainty; whereas for M664M, there does appear to be a small measurable increase in threshold current. The fractional change in slope efficiency is $2.3 \pm 0.6\%$ and $0.5 \pm 0.2\%$ for M1244D and M664M, respectively. The larger slope efficiency is actually indicative of improved laser performance; however, this increase is within the typical measurement uncertainty represented by the red dashed lines in Figure 12. Furthermore, the most significant change in slope efficiency was observed after the second radiation step for all three lasers, including the control laser. Thus, this increase could just result from a change in the measurement set-up.

Table 8. Results for the QCLs Showing the Measured Average Threshold Current and Slope Efficiency Prior to and After Each Gamma Dose of 500 krad(Si). Uncertainties are $\pm 2\sigma$.

	Average Threshold Current (mA)	Average Slope Efficiency (mW/A)	Number of Trials	Dates
M1244D				
Before gamma dose	461.3 ± 0.3	1744.1 ± 6.6	7	7/29–8/01
After 1st gamma dose	461.7 ± 0.5	1743.5 ± 6.9	8	8/05–8/12
After 2nd gamma dose	462.2 ± 0.4	1776.3 ± 7.6	7	8/15–8/21
Before 3rd gamma dose	461.6 ± 0.2	1777.3 ± 31.8	7	9/10–9/16
After 3rd gamma dose	461.8 ± 0.5	1783.5 ± 7.4	8	9/17–9/26
M664M				
Before gamma dose	669.0 ± 0.6	469.2 ± 0.9	8	7/22–8/01
After 1st gamma dose	670.1 ± 0.7	468.8 ± 1.9	8	8/05–8/13
After 2nd gamma dose	672.6 ± 0.9	474.6 ± 3.4	8	8/15–8/21
Before 3rd gamma dose	671.6 ± 0.4	474.4 ± 11.4	7	9/09–9/16
After 3rd gamma dose	672.4 ± 0.8	476.3 ± 2.8	8	9/17–9/26
M577G – Control QCL1				
Before gamma dose	652.7 ± 0.6	611.0 ± 1.6	8	7/23–7/29
After 1st gamma dose	653.0 ± 1.9	613.5 ± 12.8	10	8/04–8/14
After 2nd gamma dose	652.5 ± 0.8	625.7 ± 6.0	4	8/14–8/18
After 3rd gamma dose	n/a	n/a		
M665B – Control QCL2				
Before gamma dose	n/a	n/a		
After 2nd gamma dose	716.1 ± 0.6	395.5 ± 1.3	10	8/28–9/04
Before 3rd gamma dose	715.5 ± 0.4	396.3 ± 0.5	4	9/09–9/16
After 3rd gamma dose	715.4 ± 1.1	396.9 ± 2.1	8	9/17–9/26

*The control QCLs, M577G and M665B, are not exposed to any radiation. They are just tested over a similar timeframe.
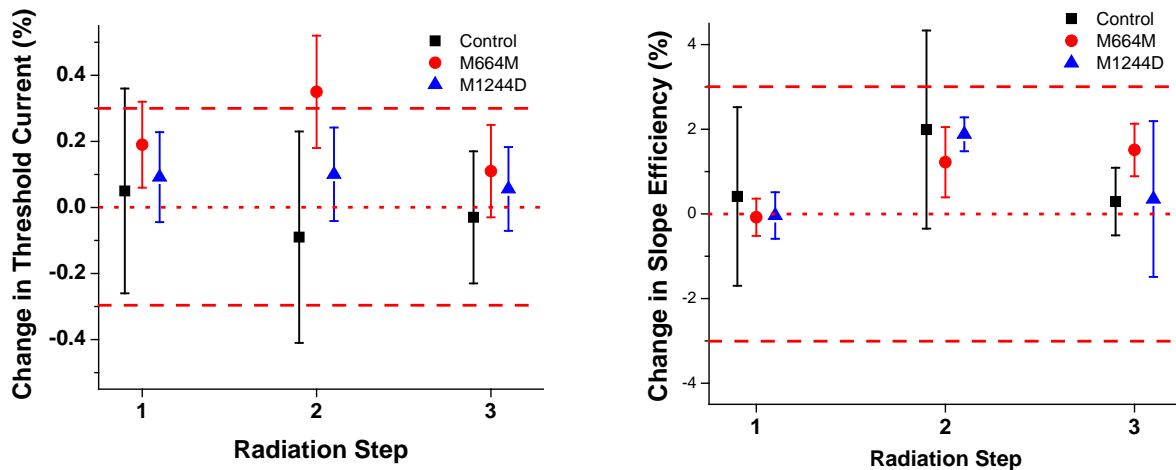
Figure 12. Fractional Change in Threshold Current (left) and Slope Efficiency (right) after Each Radiation Dose of 500 krad(Si). The red dashed lines are uncertainties of $\pm 2\sigma$ obtained using standard error propagation, and the average uncertainty determined from upwards of 60 mounting cycles of multiple QCLs.

In the next two sections, the measurements for both M1244D and M664M are presented to examine the results from the radiation exposure in more detail.

2.4.1   M1244D Measurements

The change in output power over the three gamma-radiation steps is shown in Figure 13 for M1244D. All changes in output power are within the measurement error. Most data points are the average of 7–8 measurements (see Table 8), but the third set at 1000 krad(Si) involves averages over 14 measurements.

Figure 14 shows both the average threshold current and slope efficiency for M1244D before and after each radiation dose. Although the change in threshold current for M1244D is within the measurement uncertainty, a slight bias towards increasing threshold current is observed, and a linear fit to the data can be performed. The fit has a correlation coefficient of 0.72 and a measured slope of 0.0004 mA/krad(Si). This slope suggests that a one Mrad(Si) gamma exposure could show an increase in threshold current of 0.4 mA. In the next year the same set of QCLs will be exposed to a high gamma dose to help determine if the small change in threshold current is due to radiation exposure, measurement uncertainty, or damage through handling of the devices.
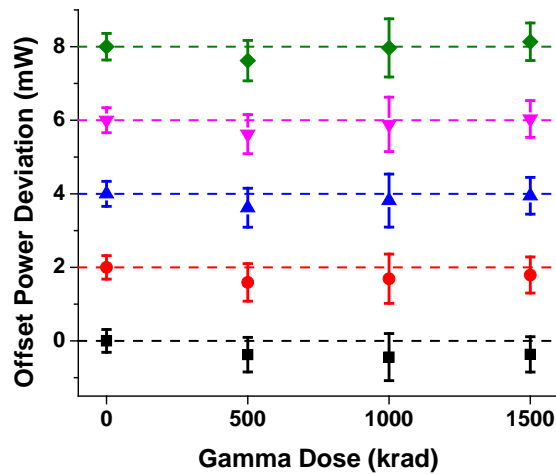
Figure 13.   Relative Power Deviations for M1244D as a Function of Gamma Dose. The error bars represent ±2σ.
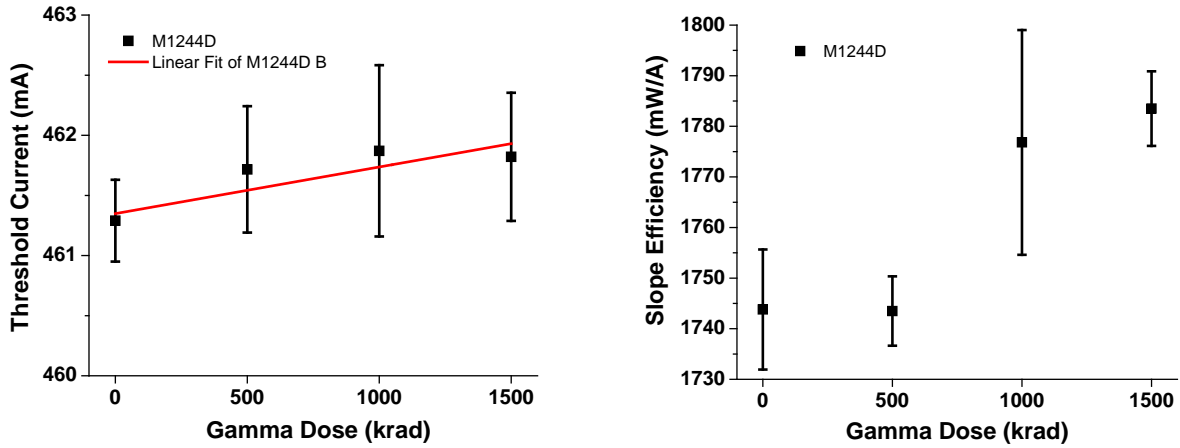
Figure 14.   The Average Threshold Current (left) and Slope Efficiency (right) as a Function of Gamma Dose. The error bars are reported as ±2σ.

2.4.2   Performance of M664M

Similarly, the change in output power over the three gamma-radiation steps is shown in Figure 15 for M664M. Most measurements are the average of 7–8 trials (see Table 8), but the third set of measurements at 1000 krad(Si) involves 15 trials that were averaged together. For this QCL, a slight decrease in output power is observed for all of the current levels.
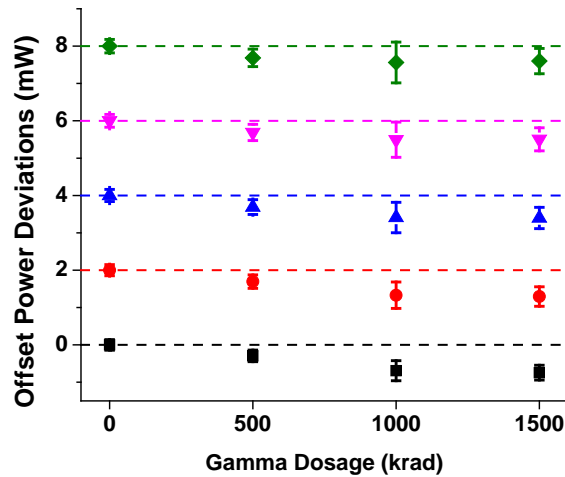
Figure 15.   Relative Power Deviations for M664M as a Function of Gamma Dose. The error bars represent ±2σ.

Figure 16 shows the average threshold current and slope efficiency before and after each radiation dose. An increase in threshold current is observed with each radiation dose, and a linear fit to the data can be performed. The fit has a correlation coefficient of 0.95 and a measured slope of 0.0024 mA/krad(Si).

This slope suggests that a one Mrad(Si) gamma exposure could show an increase in threshold current of 2.4 mA. This change should be measurable and provide a better indicator of radiation damage. Next year, we plan to expose this QCL (in addition to M1244D discussed in the last sub-section) to a much larger radiation dose; that is, 1.5 Mrad(Si).
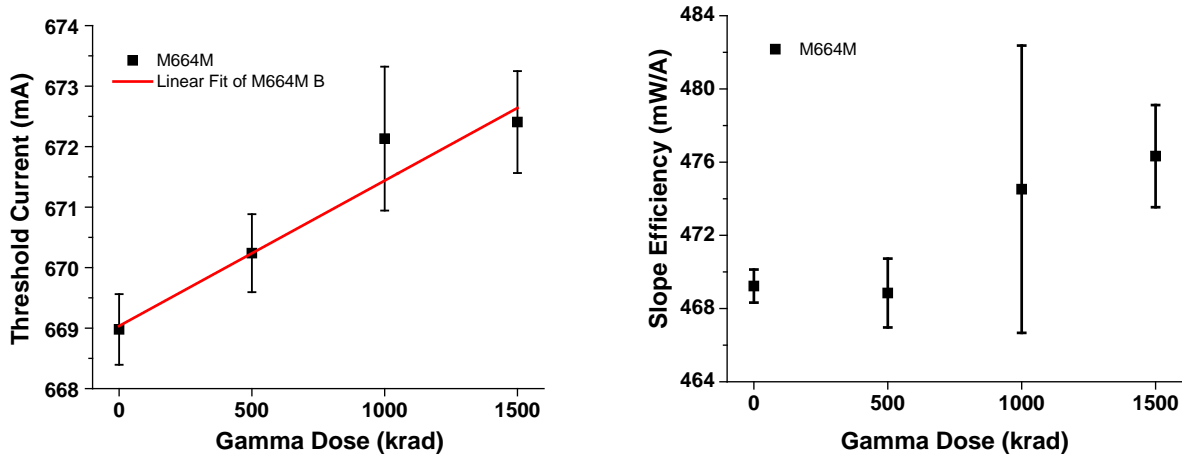
Figure 16. The Average Threshold Current (left) and Slope Efficiency (right) for M664M as a Function of Gamma Dose. The red line is a linear fit to the experimental data.

2.5   Thermal Contact

2.5.1   C-Mount versus CS-Mount

USU attached an external thermistor to the C-mount for one of their QCLs to monitor the temperature closer to the QCL active region. Extreme care must be taken because any fumes created by soldering or epoxies can deposit on the facets and cause laser damage. Thus, we chose not to pursue this path and just use data from USU. Data from the USU QCL testing station is shown below in which the internal thermistor of the ILX mount is controlled to 20.00°C. A thermal load was imposed on the C-mount, by ramping the current to the QCL over nine different levels in 20-second long steps; the first two current levels are below threshold, and the current is increased by 50 mA with each step; the initial current is 438 mA, and the final current is 837 mA. Figure 17 shows the temperature of the C-mount increased relative to the temperature of the internal thermistor. With the first current step, the temperature increased 2.15°C to 22.15°C, and then increased about 0.33°C for each subsequent step so that the final temperature was 24.8°C demonstrating an increase in temperature of 4.8°C. These results show that although the laser mount temperature is controlled to 20°C, the C-mount temperature is quite higher and therefore may be especially sensitive to minor changes in thermal contact that can occur from dismounting and remounting as well as degradation of the surface.
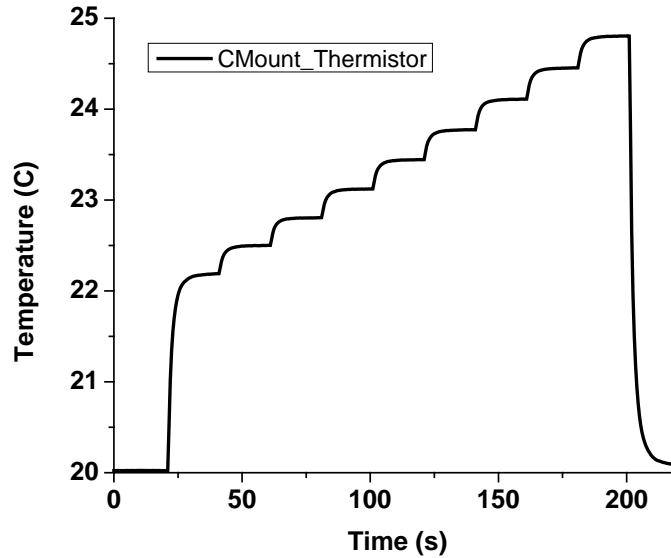
Figure 17.   Temperature Rise of Thermistor Mounted on C-mount. The temperature is controlled to 20°C on laser mount and the current to the QCL is ramped over nine steps.

2.5.2   CS-Mount

PNNL started testing a QCL from Adtech Optics that is mounted on a CS-mount with a thermistor attached, as shown in Figure 18. The CS-mount is larger than the C-mount and measures around $1\times1\times0.25$ in^3. These tests were aimed to determine if better repeatability in the threshold current and output power might be achieved when the laser is dismounted and reattached to the temperature-controlled mount. Initial tests showed good agreement between the internal thermistor of the ILX temperature-controlled mount with the external thermistor attached to the CS-mount. Turning on the QCL also did not show a large temperature difference between the external and internal thermistors. When the thermoelectric cooler was set to 20.00°C for the internal thermistor and a cw current of 750 mA was applied to the QCL, the external thermistor read a temperature of 20.66°C. Similarly, when the laser was modulated at 40 kHz, with a peak current of 800 mA applied to the QCL, the external thermistor registered a temperature of 20.66°C.

We tested the repeatability of the output power, threshold current, and slope efficiency of the CS-mounted QCL, CS-10-35HR, over eight dismount-remount trials. The results are shown in Table 9 for this, and two other QCLs on standard C-mounts, M665B and M577G. The temperature was controlled using the internal thermistor for the ILX temperature-controlled mount for all three QCLs. The uncertainty in the measured output power for all five current levels was reduced for the QCL mounted on a CS-mount by about a factor of two. The uncertainty in the threshold current was also reduced by at least a factor of three. Little change was observed in the slope efficiency. In the next quarter, we plan to use the external thermistor on CS-10-35HR to control the set point temperature to determine if even better repeatability can be obtained.
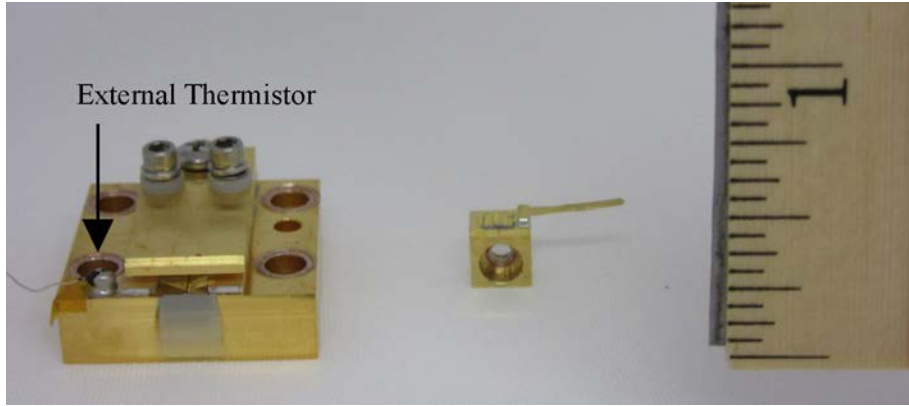
Figure 18.   Photograph Comparing the Larger CS-mount with an Attached Thermistor to the Smaller C-mount Alongside a Ruler for Scale

Table 9.   The Measured Output Power (P) for Five Current Levels above Threshold (R2-R6), the Calculated Threshold Current and Slope Efficiency; the Absolute and Relative 2σ-Uncertainties are Also Shown, for a QCL Mounted on a CS-mount (CS-10-35HR) and Two QCLs Mounted Standard C-mounts (M665B and M577G)

	R2 (mW)	R3 (mW)	R4 (mW)	R5 (mW)	R6 (mW)	Threshold Current (mA)	Slope Efficiency (mW/A)
CS-10-35HR							
Average	6.379	12.874	19.025	24.823	28.938	681.878	1104.219
2 × Std. Dev.	0.107	0.157	0.168	0.155	0.149	0.224	3.108
2 × Rel. Std. Dev.	1.68%	1.22%	0.88%	0.62%	0.51%	0.03%	0.3%
M665B							
Average	6.927	12.780	18.719	24.330	28.151	715.380	396.882
2 × Std. Dev.	0.279	0.297	0.322	0.349	0.367	1.264	2.097
2 × Rel. Std. Dev.	4.0%	2.3%	1.7%	1.4%	1.3%	0.2%	0.5%
M577G							
Average	6.174	11.970	17.924	24.002	28.162	652.715	610.975
2 × Std. Dev.	0.210	0.227	0.236	0.259	0.266	0.638	1.610
2 × Rel. Std. Dev.	3.4%	1.9%	1.3%	1.1%	0.9%	0.1%	0.3%

3.0   Beam Homogenization for QCL Source System

This project seeks to replace the use of blackbody sources as secondary calibration sources for infrared instruments in airborne or space-borne applications. The working approach to the project is to combine at least three QCL sources that can be selected by the user to illuminate the instrument under calibration for radiometric calibration (and perhaps wavelength calibration). Earlier project results focused on the use of packaged and collimated sources for several reasons: (1) they were developed under previously funded projects and could be repurposed and (2) collimated sources provided a flexible source to either couple into fibers or integrating spheres.

Careful testing revealed that the Germanium collimating lenses of the packaged lasers could alter the modal characteristics of the Fabry-Perot lasers (it actually improved their modal purity) and that the package window could offer variable amounts of optical feedback depending on the package temperature to cause instability in laser power and wavelength. This latter effect required a second temperature servo to ensure the package could be maintained at a constant temperature. Although there are valid reasons why the packaged laser approach was initiated, it became apparent that because we aim to produce a homogeneous and uniform intensity beam emitted at a specified solid angle, there was no real reason to collimate the laser as the introduction of optical elements in the beam path provided additional opportunities for optical feedback, which impacts laser power and wavelength stability. Therefore, our current approach is to inject the diverging output of each laser into non-imaging beam-homogenization and shaping elements, in order to convey the laser output to the device under calibration.

3.1   Laser Characteristics

Earlier work characterized the output of some FP lasers, both in raw emission profiles as well as the beam propagation metric M^2 (Krishnaswami et al. 2008). For this work, we found the full width at half maximum (FWHM) for a typical FP laser to be $62° \pm 2°$ and $32° \pm 2°$ for the fast and slow axes, respectively. These correspond to $1/e^2$ points of $52.7°$ (fast axis) and $27.2°$ (slow axis), respectively; these values are used as typical emission properties of the QCL. Emission sources having the fast and slow axes divergence of the measured lasers were created in TracePro for subsequent design and modeling having angular distributions as stated earlier with respect to $1/e^2$ points and flux weighted in proportion to the angular emission profile of the source.

3.2   Beam Homogenization Approaches

The approach to beam homogenization is focused on the use of hollow light pipes for mixing, as well as the use of integrating spheres. To tailor the divergence of the output of either device, cones or compound parabolic concentrators are envisioned because of their high throughput or étendue. However, there is little in the literature on the use of raw laser output as the input to either light pipes or integrating spheres, so both methods must be investigated and approaches to mitigate some of the problems unique to asymmetric laser sources must be employed.

3.2.1 Integrating Sphere Method

The initial method focused on injecting the collimated output of three laser sources into an integrating sphere and transforming the output emission angle of the sphere using a compound parabolic concentrator. For the native emissions of the QCLs some method must be employed to eliminate the possibility of light directly exiting from the exit port of the integrating sphere as well as single scattered rays, which give rise to inhomogeneity in the output intensity and produce hot spots in the output intensity profile. The solution pursued to eliminate this effect is to inject the laser light through a rectangular beam homogenizer in combination with strategically placed baffles inside of the sphere.

3.2.2 Beam Homogenizer Input

The input lasers are homogenized initially using a rectangular, hollow, tapered-beam homogenizer (also called lightpipes or mixing rods) with a starting cross section of 12.7 mm × 12.7 mm, which tapers outwardly to a final dimension of 12.7 mm × 25.4 mm, with the long dimension transverse to the optical axis of the exit port of the integrating sphere. The interior surface is diffusely reflecting. The length of the tube is 76.2-mm long. According to Cassarly (Cassarly 2012), rectangular lightpipes provide more uniform output and tapering can preserve étendue and alter the divergence/emission angle of the exit surface of the lightpipe. The length was arrived at empirically, but a general rule of thumb is that longer lightpipes minimize any structure in the output intensity. The output of the tapered homogenizer is shown in Figure 19.
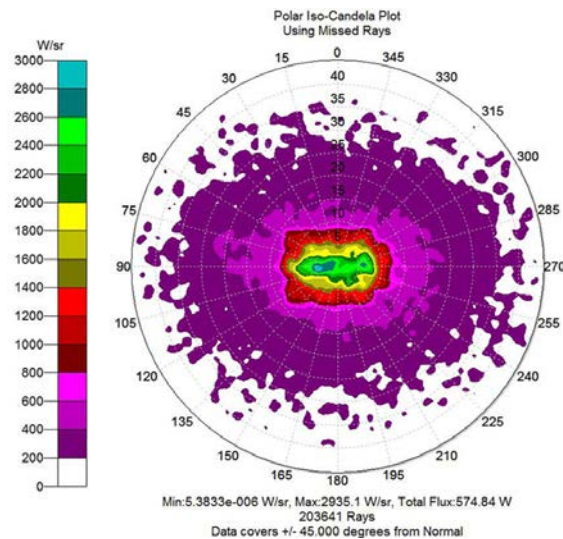
**Figure 19**. Hemispherical Emission of the Tapered Light Guide Described in the Text Showing the Asymmetric Emission

The emission profile cross sections of light exiting the CPC are shown in Figure 20. The effect of the asymmetric taper can be seen in the hemispherical plot of Figure 19 illustrating the reduced angular divergence in the direction towards the exit port (FWHM is approximately ±6.5°) and the intensity is

$1/25^{th}$ the peak value at ±40°. This reduces the possibility of direct rays or single scattered rays from exiting the sphere and CPC and creating hot spots in the output intensity distribution.
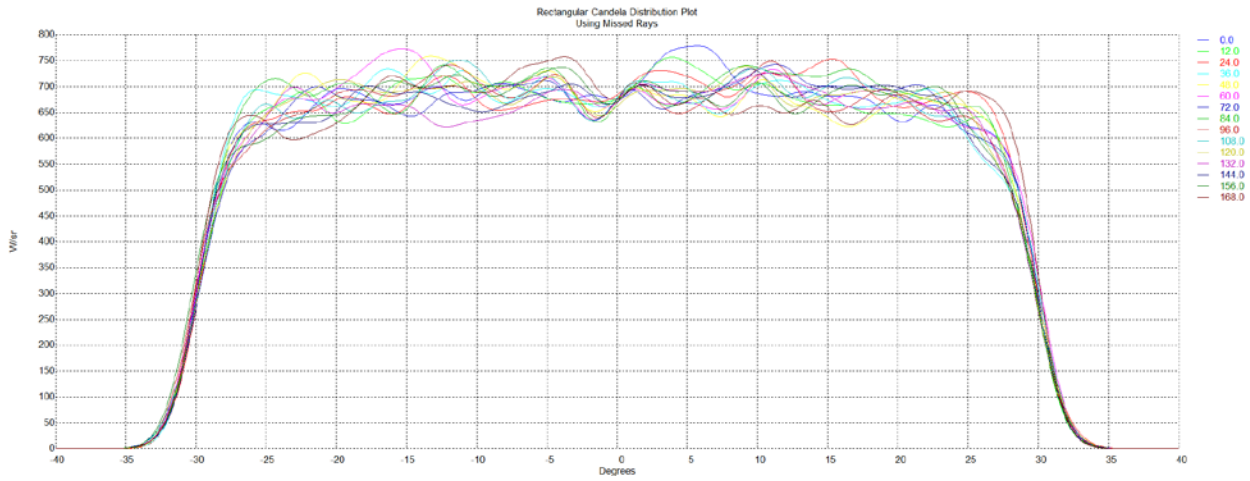
Figure 20.   Cross Section Output of the Exit of the Integrating Sphere CPC with <u>No Baffling</u> Inside the Integrating Sphere. The different traces are cross sections of the exiting beam at various azimuthal orientations of the beam cross section.

Without the baffle, there is a small quantity of single scattered rays that exit the CPC, as can be seen on the intensity distribution of rays on a dummy surface placed at the exit port of the CPC that shows only those rays that have been scattered once before they reach the exit. The ray distribution is depicted in Figure 21. The irradiance distribution for all rays due to the system is shown in Figure 22, with an estimated efficiency of 52%.
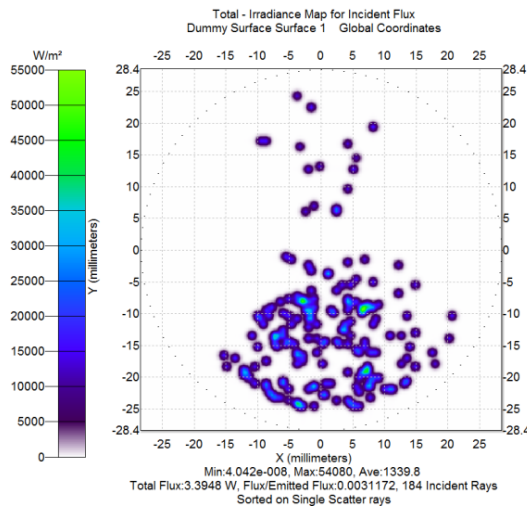
Figure 21.   Rays Sorted to Show Only Those Having Single Scattered Arriving at the Exit Plane of the CPC. Only 184 single-scattered rays escape out of 300,000 originally launched or 0.061%.
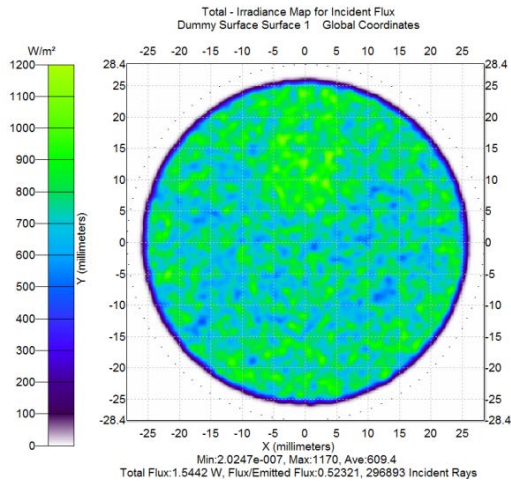
Figure 22.   Irradiance Distribution at the Exit Surface of the CPC for the Tapered Lightguide – Integrating Sphere – CPC System. Note that the efficiency is estimated at 52%. This assumes 99% specular surfaces and a 99% reflectance integrating sphere.

When we look at the output of the CPC mated to the integrating sphere with the addition of an elliptically-shaped suspended baffle, we see somewhat reduced uniformity (especially at the margins) in Figure 23 and so conclude that we can likely dispense with a somewhat complicated baffling approach, although the baffle-less case permits a small quantity of single scattered rays to make their way to the observation plane.
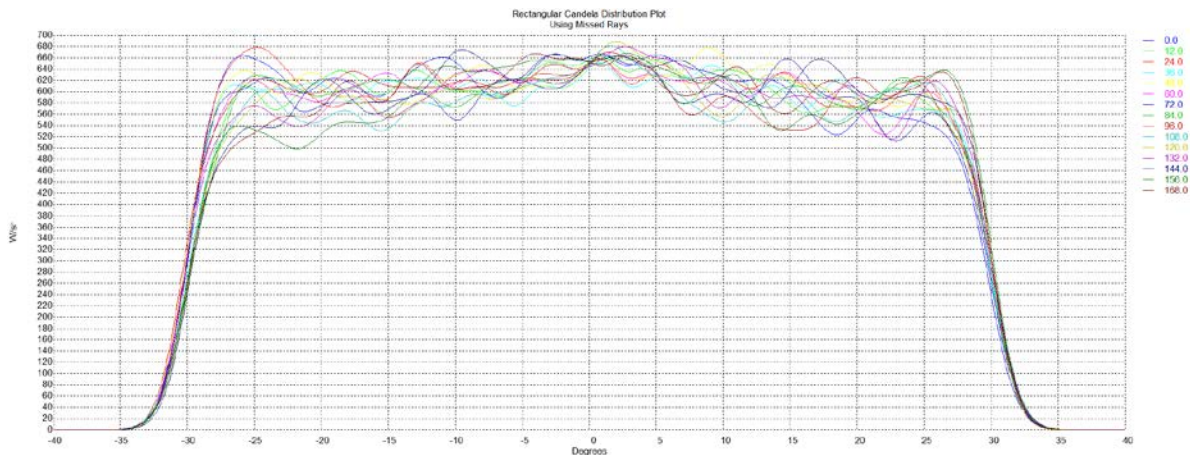
Figure 23.   Cross Sectional Output of the CPC with the Addition of a Suspended Elliptically-Shaped Baffle Mounted on the Interior of the Integrating Sphere. Note that the output uniformity is somewhat worse than the case shown in Figure 3, which leads to the conclusion that the baffle is not required when using a rectangular lightpipe at the input.

The complete lightpipe-integrating sphere-CPC system is shown in Figure 24, and includes the depiction of the baffle shape and location, if desired.

3.4
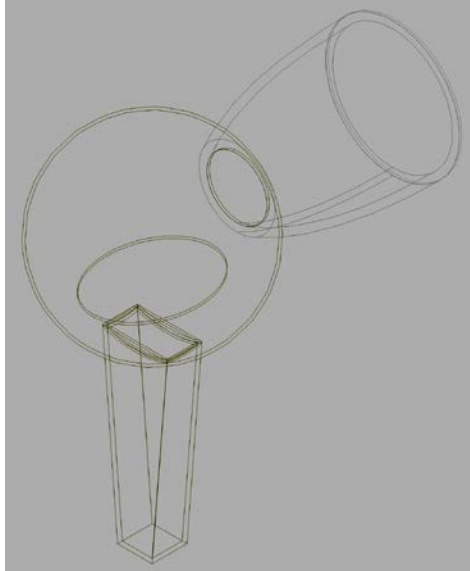
Figure 24. Perspective View of the Complete Assembly for Transformation of the Intensity Profile of 3 QCL Lasers with Initial Homogenization Using a Tapered Rectangular Lightpipe, 76.2- mm-diameter Integrating Sphere with two 25.4-mm Ports, and a CPC that Maps the 2π Output of the Sphere into $\pm30°$ and 50.8-mm Output Diameter Exit Beam. The size and location of the suspended baffle is also shown, and may be optional because the amount of singly scattered light exiting the sphere with no baffle is negligible.

Finally, the output distribution in the hemispherical plot of Figure 25 shows the nominal $\pm30°$ output of the CPC and uniform intensity profile from the tapered rectangular lightpipe, integrating sphere, and CPC.
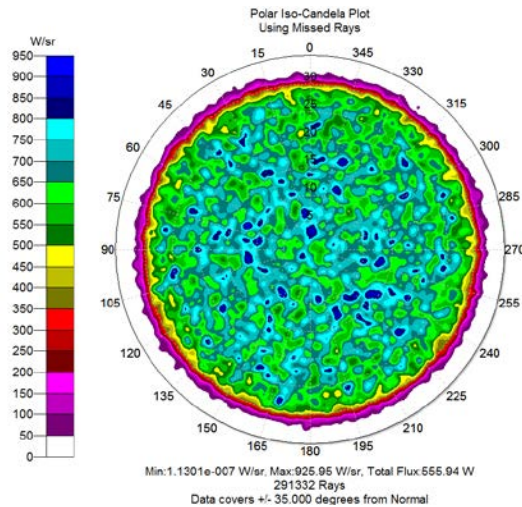
Figure 25. Output of the CPC Mapped onto a Hemispherical Surface Showing the Relatively Uniform Output of the QCL-Lightpipe Integrating Sphere-CPC System Diverging at $\pm30°$

3.3 Tapered Lightpipe and CPC

A reasonable question arises as to whether one can dispense with the integrating sphere in the interest of compactness and simplicity. To that end, a design was undertaken that utilizes only a homogenizer lightpipe and CPC. In this example, the lightpipe is symmetrically tapered (flared) from 12.7 mm × 12.7 mm to 25.4 mm × 25.4 mm, and then mated to a rectangular CPC.

Additionally, several designs were investigated, starting with a CPC emitting ±30° as well as a second design emitting at ±15°. One complication to using a CPC to reduce the angular divergence is the unavoidable design reality that the smaller the desired divergence angle or numerical aperture (NA), the longer the CPC must be. For a 25.4-mm input, a properly designed CPC to emit at ±15° will result in a design having a length of 231 mm. Compare this with the 30° emitting CPC, which has a design length of 66 mm. Because we no longer have the contribution from the integrating sphere, the length of the lightpipe was increased to 100 mm to further homogenize the beam, and its output is then mated to the rectangular CPC. Figure 26 depicts the perspective view of the first system, with 50.8 mm × 50.8 mm exit aperture.
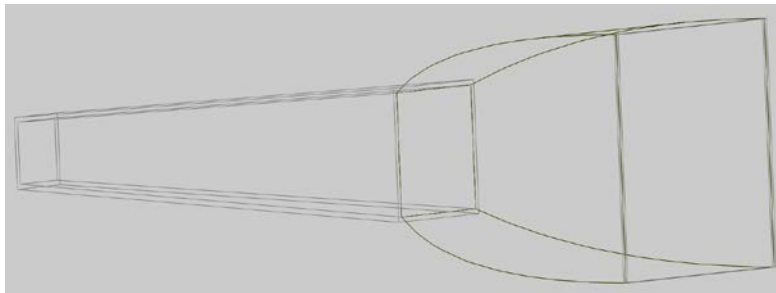
Figure 26. Silhouette View of the 100-mm-long Tapered Lightpipe Feeding the Rectangular CPC

The far-field intensity distribution for the assembly shown for the design of Figure 26 is shown in Figure 27. Because the emission from the tapered lightpipe does not emit with the distribution in ray angles produced by the integrating sphere, that is, up to 2π steradians, the re-mapping of the intensity distribution does not have the uniformity and sharp edge transitions shown in the lightpipe-integrating sphere-CPC system. Most CPC design methods assume the input of a Lambertian emitter.
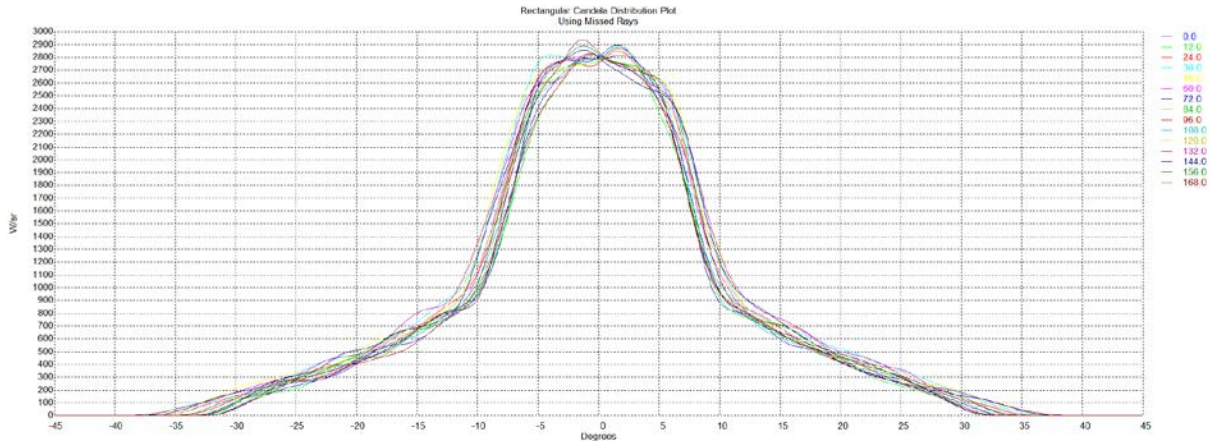
Figure 27. Intensity Cross Sections for the Output of the Rectangular CPC for a Variety of Azimuthal Cross Sections. Note that we still achieve the ±30° emission range, but with very gradual intensity transition from the peak of the response to the wings of the profile.

Not surprisingly, there are single-scattered rays that reach the exit port of the CPC. However, they are uniformly distributed, and do not appear to create obvious hot spots, as can be seen in Figure 28.
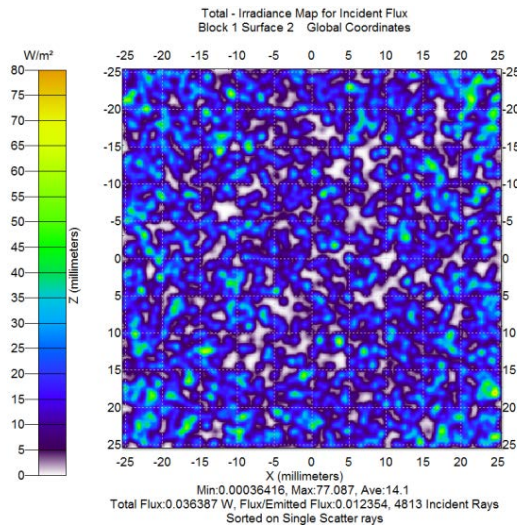
Figure 28. Plot of Intensity Distribution at the Exit Port of the Rectangular CPC Showing Only Those Rays that were Singly Scattered. The rays appear to be uniformly distributed, which suggest the singly scattered rays would not create significant localized hot spots. 900,000 rays were traced (300,000 rays per source).

We can also examine those rays that reach the exit port of the rectangular CPC that are specularly reflected. These may arise from reflection from the CPC wall, which was assigned mirror properties in the model, while the surface of the tapered rectangular cone was assigned diffusely scattering properties. This irradiance distribution can be seen in Figure 29.
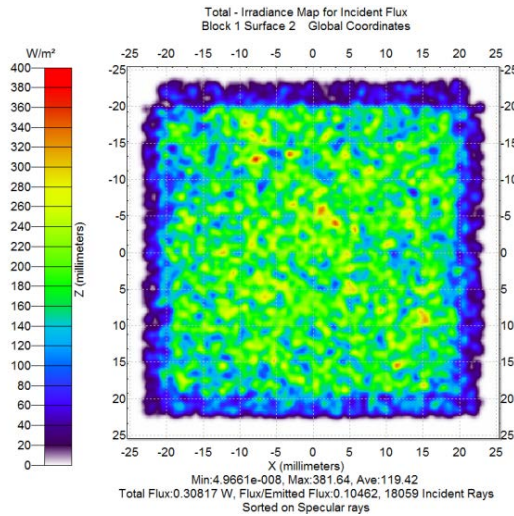
Figure 29. Irradiance at the Exit Port of the Rectangular CPC is Mapped Showing Only Those Rays that Arrive Due to Specular Reflection from the Walls of the CPC

Finally, the irradiance pattern is revealed at the exit surface of the CPC for all rays in Figure 30. Each source provides 1 W of flux, and the efficiency is 47%.
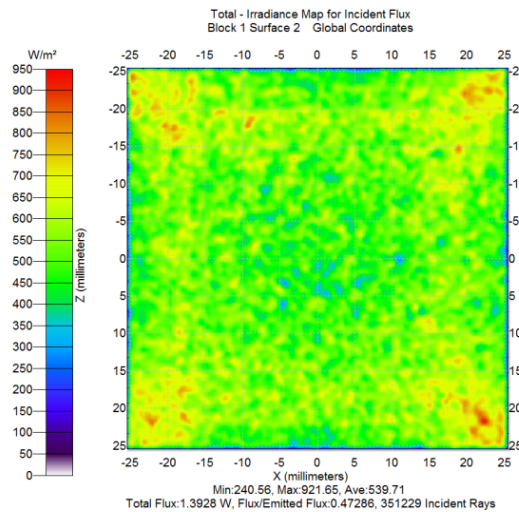
Figure 30. Irradiance Distribution for All Rays Reaching the Exit Port of the CPC. Note the four-quadrant symmetry of increased light irradiance in each corner of the pattern. The efficiency of light reaching the exit port is 47%. The mean intensity is 539.7 W/m^2 ± 84.8 W/m^2, with about 1.5% of this noise attributed to statistical noise from Monte Carlo ray tracing.

What we will eventually use is the far-field pattern from the CPC and this can be visualized in the hemispherical irradiance distribution plot in Figure 31.
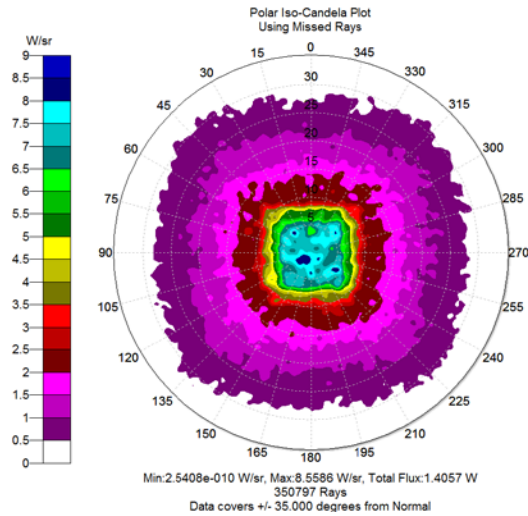
Figure 31. Hemispherical Irradiance Distribution is Shown for the Far-Field Pattern that Exits from the Rectangular CPC and Tapered Rectangular Light Guide. Note that there is uniform irradiance for ±10° although the CPC is designed to produce a ±30° beam from a Lambertian source.

A rectangular CPC was designed to emit at ±15° with an overall length of 231 mm and modeled also, but its performance in the far field is similar to the shorter CPC, with the near field at the exit port of the CPC lacking the increased intensity in the four quadrant corners, but with much reduced efficiency at 15% and much worse statistical performance exhibiting a mean intensity of 44.8 W/m^2 ± 19.0 W/m^2.

4.0   Coherence Mitigation

Traditional thermal-based calibration sources are typically extended area sources having Lambertian emission properties, meaning they emit with the same radiance or brightness when viewed from any angle. The output of these calibration sources can be modified by optics and/or baffling to emit from a solid angle that matches the F-number of the instrument to be calibrated. Thermal sources are also randomly polarized and lack spatial or temporal coherence. These optical properties match the optical properties of most natural scenes, which make them a good match for calibration sources. QCL sources, on the other hand, are highly polarized point sources that possess temporal and spatial coherence and emit with a highly directional quasi-Gaussian output. The coherence of the QCL beam enables the beam to interfere with itself to cause speckle. Speckle can produce a non-uniform irradiance pattern in the system. A non-uniform irradiance pattern on a focal plane array can produce noise as well as false irradiance levels and must be mitigated in some way. Polarized light emitted from the QCL has the potential to be transmitted through the sensor optics differently than the light from the natural scene and therefore result in calibration errors. For these reasons, the QCL source must be transformed to have a uniform output with reduced coherence effects (speckle) and random polarization.

We mitigate the coherence of the QCL beam by frequency chirping of the QCL to decrease the coherence of the laser on the scale of the observed laser speckle. In FY13, a brass board demonstration and evaluation system was constructed to inject the light from three QCLs into a 3-inch-diameter integrating sphere (Bernacki et al. 2013). In this way, the light emitted from the exit port of the sphere will have uniform intensity and emit into a solid angle of 2π steradians. Each laser was housed in a commercial high heat load (HHL) package with collimation optics within the package including an exit window, then coupled via free space optics (turning mirrors) into the 1-inch-diameter entrance port of the two-port sphere. This brass board is used to monitor the speckle from the output of the integrating sphere to verify if the output beam has the desired Lambertian qualities and has minimal speckle.

4.1   Experimental

A FLIR A655sc microbolometer IR camera is used to view the output from the integrating sphere. The IR camera has a resolution of 640×480 pixels and a frame rate of 50 Hz. The output from the integrating sphere was imaged off a 2-inch mirror that is approximately 10 cm from the 3-inch-diameter integrating sphere (unless otherwise noted). Two images are recorded with the camera: one image is recorded with the current to the laser on (see the left panel in Figure 32), and a background image is recorded with the current to the laser off (see the middle panel in Figure 32). The background image is subtracted from that with current on, to produce the background subtracted image shown in the right panel for Figure 32. When recording these images, the minimum and maximum values for the scale limits were determined from the image with the laser in operation; then, the limits are locked so they do not change for the image with the laser turned off.
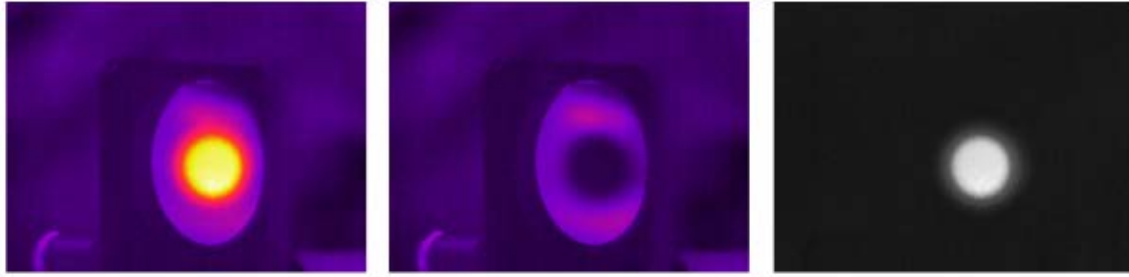
Figure 32. Images from Output of the Brass Board System and an Integrating Sphere with 1-inch Output Port. The left panel shows the image with the current to the laser on; the middle panel shows the background image recorded with the laser current off; and the right panel shows the background subtracted image also called the processed image (current on – current off).

4.2   Comparison of CW versus Modulated Current

4.2.1   M784C

The output from the standard integrating sphere using a distributed feedback QCL, M784C, was compared for two operating modes, cw operation with a current of 750 mA, and modulated operation using a 40-kHz modulation frequency with a peak current of 750 mA. Figure 33 shows the processed images with cw current (left) and with modulated current (right) demonstrating that modulating the current to the QCL reduces the speckle noise observed on the camera quite significantly. Table 10 shows the average, standard deviation, and relative standard deviation for a 26×26 pixel spot size in the center of the processed images in Figure 33. Similarly, the standard deviation is calculated in the center of the background image. To estimate the speckle noise, we subtract the standard deviation from the background image from the processed image using propagation of errors such that $\sigma^2 = \sigma_{processed}^2 - \sigma_{bckgrd}^2$; this new standard deviation is used to estimate the speckle noise in the processed image and is shown in Table 10. Thus, modulating the QCL at 40 kHz reduces the speckle noise by more than a factor of 20.
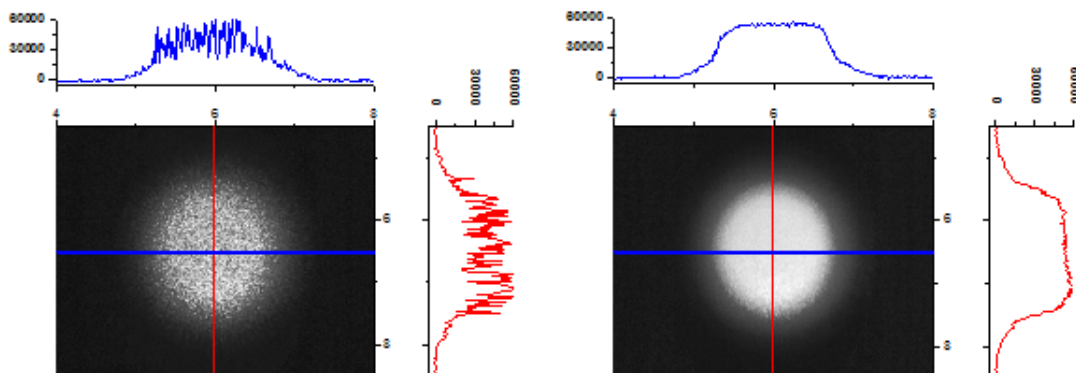
Figure 33. Background Subtracted Images from the Output of the Brass Board System and an Integrating Sphere when M784C is Operated cw (left) and when the Laser is Modulated at 40 kHz (right)

Table 10. Estimated Speckle Noise for Both 40-kHz Modulation and cw Operation for M784C

	40 kHz	cw
Average	53689.24	41901.55
Standard Deviation	1767.773	11413.84
2 x Relative Standard Deviation	3.3%	27.2%
Estimated Speckle Noise	1.2%	27.0%

4.2.2   M664L

The output from the standard integrating sphere using a FP QCL, M664L, is also viewed at different modulating frequencies to determine the optimal modulation frequency. The processed images are shown in Figure 34 using a peak current of 750 mA.
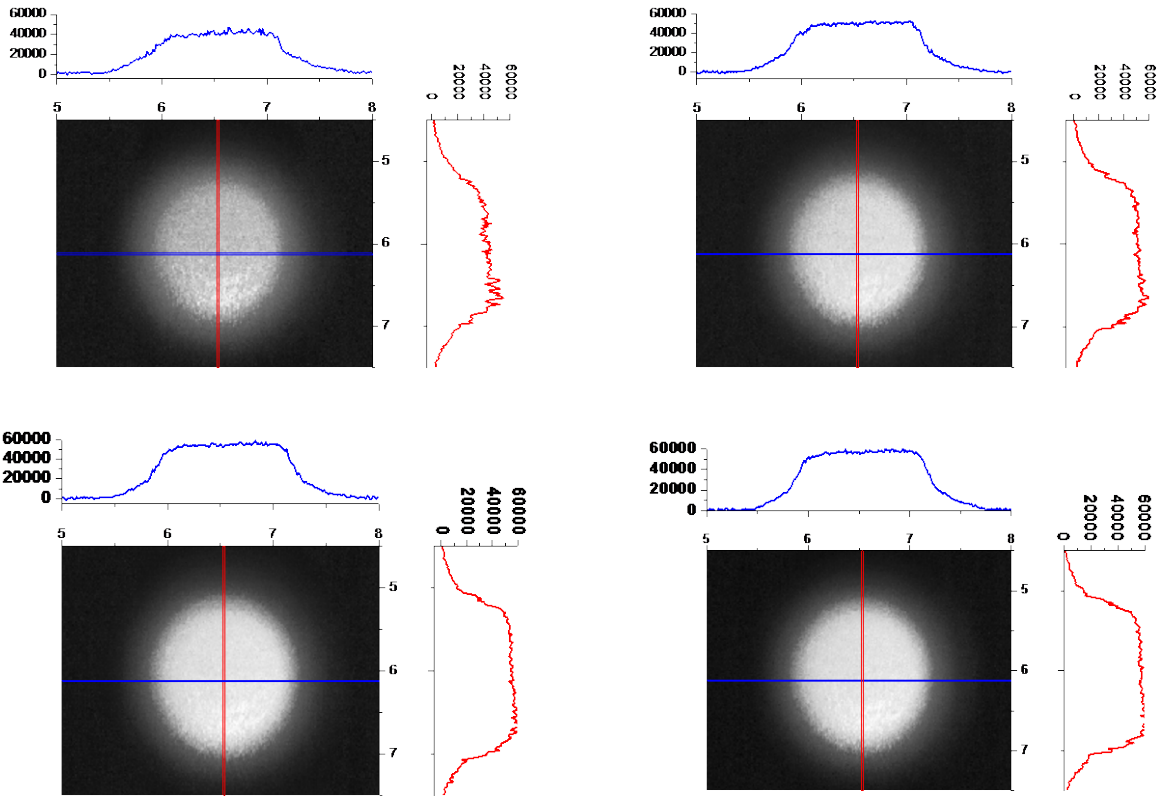
**Figure 34**.   Background Subtracted Images from the Output of the Brass Board System and an Integrating Sphere when M664L is Operated at Various Modulation Frequencies: 10 kHz (top left), 40 kHz (top right), 100 kHz (bottom left) and 200 kHz (bottom right)

Table 11. Estimated Speckle Noise for M664L at Various Modulaiton Frequencies

	10 kHz	40 kHz	100 kHz	200 kHz
Average	40861.1	50533.58	54531.14	56641.89
Standard Deviation	2491.687	1567.046	1276.529	1293.453
2 x Relative Standard Deviation	12.2%	6.2%	4.7%	4.6%
Estimated Speckle Noise	10.7%	4.1%	1.8%	1.9%

The speckle noise does change with modulation frequency. Increasing the modulation frequency further reduces coherence so that we might need to consider increasing the modulation frequency to >40 kHz.

5.0 CPC Performance

The output from the integrating sphere will not be used without some beam transformation to reduce the emitted solid angle in order to match the F-number of an instrument under calibration, and thus, the integrating sphere's output will be coupled through a non-imaging compound parabolic concentrator to reduce its divergence but maintain the étendue or throughput of the instrument. A CPC was constructed for the brass board system and is shown in Figure 35. The length of the CPC is 70 mm and the diameters of the input and exit apertures are 25.4 mm and 50.8 mm, respectively.

Figure 35. Photograph of the CPC that is Used to Reduce the Divergence of the Output from the Integrating Sphere to ±30°

Images were recorded to show the CPC transforms the image from the integrating sphere. Figure 36 compares the processed images that are recorded off a mirror that is positioned 25.5 inches away from the output port of an integrating sphere. The integrating sphere for these measurements has been modified to optimize the baffle position in order to reduce single scattered light from exiting the sphere.
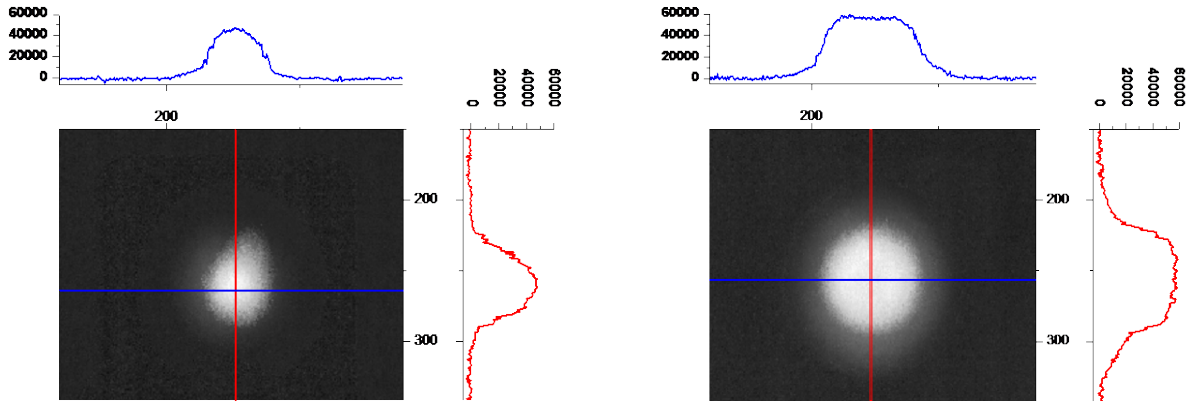
Figure 36. Background Subtracted Images from the Output of the Brass Board System Using a Custom Integrating Sphere without (left) and with (right) a CPC Coupled to the Exit Port of the Integrating Sphere. The image is recorded off a mirror positioned approximately 25.5 inches from the integrating sphere output port. M664L is modulated at 40 kHz with a peak current of 700 mA. The red and blue lines are vertical and horizontal cuts used for profiles shown in Figure 37.
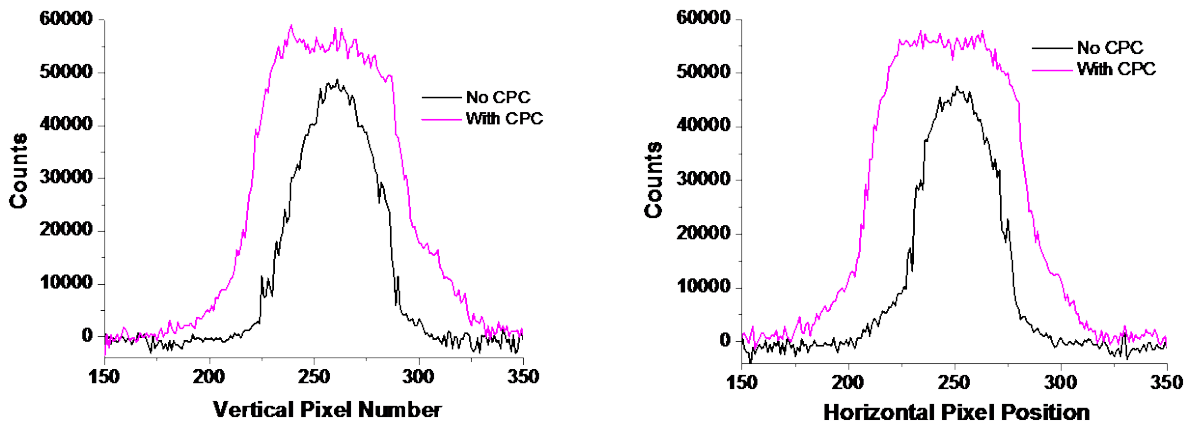

Figure 37. Vertical (left) and Horizontal (right) Cuts for Both the Outputs from the Integrating Sphere (black trace) and Integrating Sphere Coupled to a CPC (magenta trace). M664L is modulated at 40 kHz with a peak current of 700 mA. The recorded image is reflected off a mirror positioned approximately 25.5 inches from the integrating sphere output port. The vertical cut is along the horizontal pixel number 251, and the horizontal cut is along the vertical pixel number 264.

Initial analysis showed that the standard integrating sphere's internal baffle was not optimally located for collimated laser input (Bernacki et al. 2013). The baffle in a standard integrating sphere is placed between the launch port and exit port, so that its location was likely optimum for input from a widely diverging thermal light source, such as an incandescent bulb and reflector. However, when using collimated laser light injected at the sphere's south pole, it simply strikes the inner sphere wall at its north pole, allowing for some of this light to exit the sphere after only one reflective/scattering bounce from this

surface. This single-bounce condition does not allow for the random scatter from the sphere's interior walls, necessary to provide the desired uniform intensity output from the exit port. To avoid this, we obtained a custom integrating sphere in which the internal baffle was translated 90° from the stock location (i.e., the baffle is located at sphere surface between the exit port and the initial surface of incidence for the QCL beams) to frustrate single-bounce light from exiting the sphere, and this modification enabled the appropriate scattering to produce the desired output intensity distribution. This effect was easily observed with the CPC. Figure 38 shows the processed images using both the standard (left panel) and custom (right panel) integrating spheres along with the CPC. With the standard integrating sphere, a bright spot is observed in the image and is most likely due to single scattered light exiting the sphere so the intensity output is not uniform. The modified integrating sphere with the baffle in the proper location reduces this single scattered light providing a more uniform output as shown in the right panel of Figure 38.
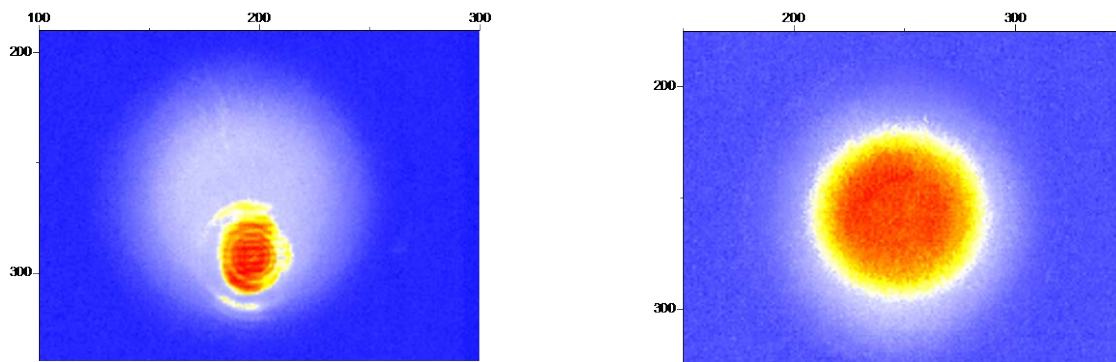

Figure 38.   Processed Images from the Output of the Brass Board System Using a Standard (left) and Modified (right) Integrating Sphere Coupled to a CPC. The image is recorded off a mirror positioned approximately 25.5 inches from the integrating sphere output port. M664L is modulated at 40 kHz with a peak current of 700 mA.

For all of these tests, we are using the brass board system built in FY12, which uses collimated QCLs (Bernacki et al. 2013). For the source system design, however, we propose to use direct injection in order to reduce optical feedback effects (Bernacki et al. 2014). Preliminary tests using a QCL on a C-mount (which produces uncollimated output) directly injected into an integrating sphere do show inhomogeneity in the output intensity, both with and without a CPC, as seen in Figure 39.
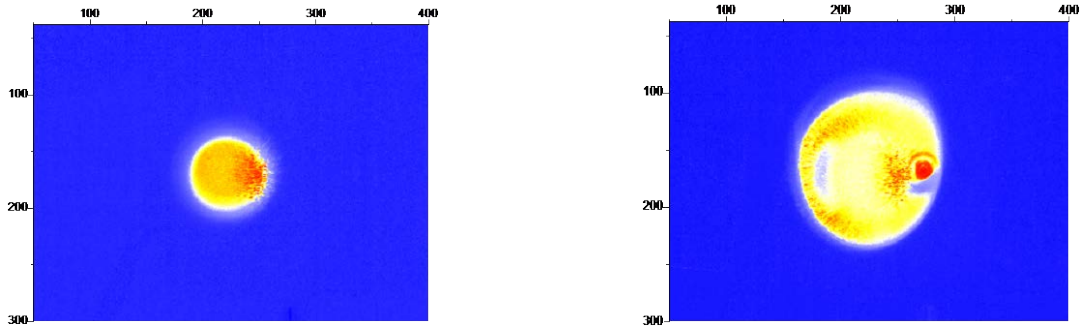
Figure 39. Background Subtracted Images from the Output of an Uncollimated QCL that is Directly Injected into the Modified Integrating Sphere without a CPC (left) and with a CPC (right)

As discussed in Section 3.0, a beam homogenizer such as a rectangular light pipe or cone will be required to minimize direct reflections as well as singly scattered rays from leaving the exit port of the integrating sphere; this will reduce inhomogeneity and hot spots in the output intensity profile.

6.0   Summary and Outlook

During FY14 considerable progress was made towards understanding the response of quantum cascade lasers to radiation exposure, both to protons and gamma rays. It was determined that moderate amounts of radiation commensurate with that likely to be accumulated during a four- to six-year space mission do not injure the performance of these devices. Any potential variations due to the impact of these radiation tests are masked by minor performance variations most likely due to the many mount-dismount cycles of the QCLs, necessary to perform these tests. It is also clear that the radiation exposures used during these tests did not have significant adverse effects on the QCLs. Next year, tests are planned with the same set of QCLs using higher radiation levels, to further verify the hypothesis that these devices are indeed robust and radiation hard. Additionally, a different mount, the CS-mount, which promises less compromise from repeated mount-dismount cycles, will be used for certain tests.

Also during FY14, two approaches were modeled to simultaneously couple the outputs of three QCLs beam transformation systems, which homogenize and randomize the light to be suitable for radiometric and wavelength calibration purposes. The first employed an integrating sphere somewhat conventionally to homogenize the laser intensity profiles, in addition to a compound parabolic concentrator to reduce the divergence of the light exiting the sphere. To ensure efficient coupling of the QCLs into the sphere, a tapered light guide input was designed to minimize the probability that direct and single scattered rays could exit the sphere and create hot spots in the intensity profile. Although the use of a suspended baffle was investigated (which allowed no rays to exit prematurely), these single scattered rays in the absence of a baffle accounted for only 184 out of the nearly 300,000 rays that exited the system after the ray trace completion.

The second approach used a tapered rectangular light guide coupled to a rectangular CPC to see if the integrating sphere could be eliminated. This method results in a strongly linear instrument volume, which may have advantages in packaging on aircraft or spacecraft, but does not transform or homogenize as effectively as the design that uses the integrating sphere. Because the output of the tapered light guide is not Lambertian, the CPC does not efficiently transform the emission profile into a restricted angular emission and so would require its output to be truncated to ensure uniform irradiance is conveyed to the system under test, and this would reduce its efficiency if laser power is an issue. Additionally, to increase the homogenization provided by the tapered light guide, its length must be increased, which may be objectionable in some applications. In FY15, the source system will be built and tested based on the first approach.

7.0   References

Bernacki BE, CS Brauer, BD Cannon, TL Myers and MS Taubman. 2014. *Annual Report for the QCL Calibration Project*. PNNL-23163, Pacific Northwest National Laboratory, Richland, Washington.

Bernacki BE, BD Cannon, TL Myers and MS Taubman. 2013. *Final Report for the Multi-Wavelength Infrared Calibration Source Project*. PNNL-22231, Pacific Northwest National Laboratory, Richland, Washington.

Cassarly W. 2012. "Design of Efficient Illumination Systems." The International Society for Optical Engineering (SPIE), Bellingham, Washington. SPIE Short Course Notes from Photonics West 2012.

Hofstetter D, M Beck, T Aellen and J Faist. 2001. "High-Temperature Operation of Distributed Feedback Quantum-Cascade Lasers at 5.3 μm." *Applied Physics Letters* 78:396-398.

Krishnaswami K, BE Bernacki, BD Cannon, N Ho and NC Anheier, Jr. 2008. "Emission and Propagation Properties of Mid-Infrared Quantum Cascade Lasers." *IEEE Photonics Technology Letters* 20(4):306-308.

Leavitt RP, JL Bradshaw, KM Lascola, GP Meissner, F Micalizzi, FJ Towner and JT Pham. 2010. "High-performance Quantum Cascade Lasers in the 7.3- to 7.8-μm Wavelength Band Using Strained Active Regions." *Optical Engineering* 49(11):111109.

Myers TL, BD Cannon, MS Taubman and BE Bernacki. 2013. "Performance and Reliability of Quantum Cascade Lasers." In *Laser Technology for Defense and Security IX*, pp. 87330E-87330E-15. April 29, 2013, Baltimore, Maryland. DOI 10.1117/12.2015479. The International Society for Optical Engineering (SPIE), Bellingham, Washington.

Stassinopoulos EG and JP Raymond. 1988. "The Space Radiation Environment for Electronics." *Proceedings of the IEEE* 76(11):1423-1442.

Taubman MS. 2011. "Low-Noise High-Performance Current Controllers for Quantum Cascade Lasers." *Review of Scientific Instruments* 82(6):064704.

Taubman MS, TL Myers, RM Pratt, RD Stahl and BD Cannon. 2014. "Precision Control of Multiple Quantum Cascade Lasers for Calibration Systems." *Review of Scientific Instruments* 85(1):014704.